Separation and Purification Technology 367 (2025) 132950

Contents lists available at ScienceDirect

Separation and Purification Technology

journal homepage: www.elsevier.com/locate/seppur

Influence of the doping level of boron-doped diamond electrodes in the electrooxidation of polystyrene nanoplastics

R. Rodrigo, L. Muñoz, J. Bonastre, J. Molina *, F. Cases *

Departamento de Ingeniería Textil y Papelera, EPS de Alcoy, Universitat Politècnica de València, Plaza Ferrándiz y Carbonell s/n, 03801 Alcoy, Spain

ARTICLE INFO

Editor: Prof. G. Chen

Keywords:
Nanoplastics
Polystyrene
Electrooxidation
Fluorescence spectroscopy
Boron-doped diamond
Advanced oxidation processes

ABSTRACT

Microplastics and nanoplastics have arisen as contaminants of emerging concern due to the wide use of plastics, and the application of boron-doped diamond (BDD) electrodes for their removal is promising. In this study, we report the influence of BDD doping levels (500, 2500, and 10000 ppm B doping) on the electrooxidation of polystyrene nanoplastics (100 nm, 20 mg·L^{-1}). Different current densities (50, 25, 12.5, and 5 mA·cm^{-2}) have been applied to determine the best electrolysis conditions for each electrode type. In addition, hydroxyl radical (•OH), persulphate ($S_2O_8^{2-}$), and hydrogen peroxide (H_2O_2) reactive species have been determined to understand the influence of the species generated on the degradation of NPs. BDD500 electrode presents the fastest degradation of PS NPs at low current densities (12.5 and 5 mA·cm^{-2}), BDD2500 at 25 mA·cm^{-2}, and BDD10000 at 50 mA·cm^{-2}. Among oxidative species determined, $S_2O_8^{2-}$ is the one generated with the highest concentration and seems to command the degradation of PS NPs, since at 25, 12.5, and 5 mA·cm^{-2}, the electrodes that produce more $S_2O_8^{2-}$ degrade faster PS NPs. At 50 mA·cm^{-2}, the differences between the different electrodes were minimal. The highest mineralization (as measured by non-purgeable organic carbon measurements) was obtained for BDD500 at 50, 25, and 12.5 mA·cm^{-2}, and BDD2500 at 5 mA·cm^{-2}.

1. Introduction

The use of products made from different synthetic plastics has gradually increased since their creation due to attractive properties such as durability, low cost, and lightness. During 2020, 370 Mt of plastic were produced, and it is estimated that by 2050, 12,000 Mt of plastic waste will accumulate in the environment [1]. Different strategies have been proposed for sustainable plastic waste treatment and recycling to avoid damage to the environment: photolysis, pyrolysis, incineration, biodegradation, or electrolysis [2].

The degradation of plastics due to physical, thermal, environmental, and biological factors leads to their progressive fragmentation into microplastics (MPs) and nanoplastics (NPs) [3]. MPs and NPs are present in the atmosphere, terrestrial environments, and inland and marine waters, which has given rise to the 'microplastics cycle' [4]. The United Nations Environmental Program has identified MPs and NPs as one of the top ten environmental problems, and their presence in water causes significant ecological risks [5]. MPs and NPs can have different origins: pellets, paints, fabrics, cosmetic products, artificial turf, tires, water treatment plants, fishing nets, agriculture, construction industry, etc. The most used plastics are polyethylene, polypropylene, polyurethane, polystyrene, polyvinyl chloride, and polyethylene terephthalate. Therefore, they are the ones who will contribute most to the generation of MPs and NPs [6]. Recently, the European Union has restricted the incorporation of MPs in different products (cosmetics, artificial sports surfaces, detergents, fabric softeners, glitter, fertilizers, plant protection products, toys, medicines, or medical devices, to name a few) [7].

MPs and NPs are classified mainly by size (<1 μm for NPs and between > 1 and < 1000 μm for MPs), although other types of classification have been suggested [8]. The other classification parameter is the shape, which can be classified as pellets, fibers, foams, fragments, or sheets [9].

In addition, plastics incorporate additives such as plasticizers, colorants, flame retardants, or additives for protection against UV radiation [10]. These additives are not chemically bound to the plastic, so they can migrate into the environment, thus being incorporated into the food chain along with the MPs and NPs. Those organisms that feed through water filtration, such as mussels or crabs, are the first to incorporate MPs and NPs into their organism [11]. The subsequent consumption of these animals by other animals located above in the food chain implies

* Corresponding authors.
E-mail addresses: jamopue@upvnet.upv.es (J. Molina), fjcases@txp.upv.es (F. Cases).

https://doi.org/10.1016/j.seppur.2025.132950
Received 24 February 2025; Received in revised form 30 March 2025; Accepted 8 April 2025
Available online 8 April 2025

bioaccumulation of MPs and NPs. The incorporation of NPs into plants has also been demonstrated [12]. A recent study has also highlighted the large number of NPs incorporated into bottled water (accounting for around 10^5 particles per liter of water, the majority being NPs) [13]. All these sources increase the probability of MPs' and NPs' ingestion by human beings. The incorporation of MPs and NPs into the body can also occur through inhalation or via the skin. MPs and NPs pose significant human risks, such as inflammation, oxidative stress, apoptosis (cell suicide), or metabolic homeostasis, especially in the digestive tract and lungs [14].

Since MPs and NPs are a growing problem, different methods have been employed for their separation and degradation [15]:

- Physical methods (adsorption, filtration, sedimentation).
- Chemical methods (coagulation/flocculation, agglomeration).
- Biological methods (activated sludge, biofilters, biodegradation).

Most of these methods do not produce the degradation of the MPs and NPs, but rather their separation. In the case of biological processes, degradation does occur, although it is partial and prolonged [16]. In wastewater treatment plants, the removal of MPs and NPs is partial, and these installations can act as potential sources of MPs pollution in aquatic environments [17]. All this makes it necessary to search for alternative techniques to achieve their degradation.

Advanced oxidation methods have emerged as an effective alternative for degrading different emerging pollutants such as pharmaceuticals, personal care products, pesticides, flame retardants, plasticizers, endocrine disruptors, surfactants, or polycyclic aromatic hydrocarbons [18–20]. Studies have used advanced oxidation methods to degrade MPs and NPs [21]. Li et al. compared the effect of ozonation versus chlorination to remove NPs in water [22]. Cao et al. employed an MXene/$Zn_xCd_{1-x}S$ photocatalyst to achieve higher utilization of visible light to degrade polyethylene terephthalate MPs while achieving hydrogen generation [23]. Liu et al. employed Fe^{2+}-activated peroxymonosulfate and Fenton's reagent, which can form free radicals in the degradation of nylon 6 and polystyrene MPs [24]. In addition, advanced oxidation methods can be employed as pretreatment to increase MPs' surface roughness and hydrophilicity, making them more susceptible to bioassimilation [25]. However, studies on advanced oxidation processes on NPs and MPs are still scarce, and there is much room for improvement both in process efficiency and in the search for new catalysts to achieve better results; for example, the interference of other contaminants in the degradation of MPs and NPs has not been studied [26]. Advanced oxidation methods typically require catalysts either in homogeneous or heterogeneous phases, meaning they must be recovered in the case of heterogeneous photocatalysts or treated in the case of homogeneous catalysts (such as Fe^{2+} in Fenton-based techniques).

Electrochemical methods are among the advanced oxidation methods and have the advantage of using solid-state catalysts in the form of electrodes, so the catalyst does not have to be recovered and can be reused. In electrochemical methods, the only reagents used are the electron and the support salts that provide electrical conductivity (harmless sulfate or sodium chloride salts), so the treated water does not require post-treatment. As for the electrochemical treatment of water with MPs and NPs, electrochemical techniques have been little used so far. Bellagamba et al. were the first to report the electrocombustion of soluble polymers such as polyacrylates using BDD anodes [27]. Kiendrebeogo et al. have studied the degradation of polystyrene NPs and MPs mainly using boron-doped diamond (BDD) electrodes [28,29]. Lu et al. also employed BDD electrodes, and to increase the degradation efficiency of the MPs, they used sodium dodecyl sulfate as an agent promoting the generation of oxidizing species capable of oxidizing polystyrene MPs and, in turn, enhancing the interaction of these species with the MPs [30]. Mais et al. studied the electrochemical degradation of polyethylene and polyethylene terephthalate using commercial electrodes of Ti/Ru/Ir oxides produced by Magneto company in a chloride medium for 31 days, obtaining a 67 % and 75 % weight loss, respectively [31]. Ning et al. used CeO_2/PbO_2 electrodes to study the electrochemical degradation of polyvinyl chloride (PVC) MPs [32]. Miao et al. employed an electro-Fenton-based method to degrade PVC MPs using a TiO_2/graphite cathode, obtaining a 75 % decrease in the Cl content of PVC after potentiostatic electrolysis at −0.7 V vs. Ag/AgCl for 6 h [33]. The development of co-catalysts [34] has also proven advantageous in the degradation of compounds such as bisphenol-A using an electro-Fenton approach [35].

Although BDD electrodes have proven helpful in the degradation of MPs and NPs, a study evaluating the influence of the boron doping level is lacking in the literature. The present study aims to fill this gap, providing information on the degradation of PS NPs and the oxidizing species generated when using different boron doping levels (500, 2500, and 10000 ppm).

2. Experimental

2.1. Reagents and materials

All reagents used were of analytical grade.

BDD electrodes: were acquired from NeoCoat company. BDD/Si NeoCoat® electrodes with 25 x 50 x 2 mm dimensions. Substrate: p-doped, monocrystalline silicon (100 mOhm·cm), etched surface. BDD coating: p-doped, poly-crystalline, 3 μm thick. Three boron doping levels were used: 500 ppm (BDD500), 2500 ppm (BDD2500), and 10000 ppm (BDD10000). The active area of the electrodes was 20 cm^2.

For the characterization and electrolysis: polystyrene latex nanospheres (0.1 μm, 2.5 wt% dispersion in water) were acquired from Thermo Scientific Chemicals. Sodium sulfate (Na_2SO_4) was purchased from Panreac. Potassium chloride (KCl) was purchased from Merck. Hexaammineruthenium (III) chloride ($Ru(NH_3)_6Cl_3$) and potassium ferrocyanide (III) ($K_3Fe(CN)_6$) were acquired from Acrōs Organics. Potassium iodide (KI) was acquired from Carlo Erba. N,N-dimethyl-p-nitroaniline was acquired from Thermo Scientific. Potassium indigotrisulfonate was purchased from Thermo Scientific.

Solutions were deoxygenated by bubbling nitrogen (N_2 premier X50S) when needed. Ultrapure water was obtained from an Elix 3 Millipore-Milli-Q Advantage A10 system with a resistivity near 18.2 MΩ·cm.

2.2. Characterization of the electrodes by cyclic voltammetry and linear sweep voltammetry

A potentiostat/ galvanostat (Autolab PGSTAT30) was used to characterize the different BDD electrodes in a three-electrode configuration, using the BDD electrodes as working electrodes, two Ti-Pt felts (Bekaert) as counter electrodes and Ag/AgCl (3 M) as the reference electrode. The solution consisted of 0.1 M KCl / 5 mM $Ru(NH_3)_6Cl_3$ or 0.1 M KCl / 5 mM $K_3Fe(CN)_6$. The potential was cycled between 0.2 V and −0.6 V for the $Ru(NH_3)_6Cl_3$ redox mediator and −0.2 V to 0.6 V for the $K_3Fe(CN)_6$ redox mediator at a scan rate of 50 $mV{\cdot}s^{-1}$.

BDD electrodes were also characterized by linear sweep voltammetry (LSV) using the previously reported three-electrode configuration, Na_2SO_4 medium (0.03 M or 0.1 M), and different NPs concentrations (20, 40, 60, 80, and 100 mg/L). The potential was scanned between 0 V and 2.5 V at a 5 $mV{\cdot}s^{-1}$ scan rate.

2.3. Electrolysis of NPs solutions

Electrolyses of polystyrene NPs were performed in a 100 mL truncated cell using a three-electrode configuration. The working electrode was the BDD electrode (BDD500, BDD2500, or BDD10000), two Ti plates (Goodfellow) were used as counter electrodes, and the reference electrode was Ag/AgCl. The electrolysis solution consisted of a 75 mL aqueous solution of 20 $mg{\cdot}L^{-1}$ NPs (0.1 μm) and 0.03 M Na_2SO_4 as a

supporting electrolyte. Gamry 1000 potentiostat–galvanostat was used to apply the desired current density. Aliquots of 3 mL were removed at different times to measure their fluorescence, and after the measurement was performed, samples were returned to the electrochemical cell. Electrolyses continued till a ~ 90 % diminution of the fluorescence emission was achieved. Aliquots of 0.2 mL were removed at different measuring times to perform size measurements by electron microscopy techniques.

2.4. Measurement of the MPs and NPs concentration using fluorescence spectroscopy

Fluorescence spectroscopy determination of NPs concentration in the different samples was carried out using a Photon Technology International spectrofluorometer, employing an excitation wavelength of 230 nm and an emission range of 260–600 nm (recorded within 1.0 nm interval) using quartz cuvettes for fluorescence. The voltage of the photomultiplier was set to 1 V.

2.5. Determination of reactive oxidative species

2.5.1. Hydroxyl radical (•OH)

Hydroxyl radical generation was monitored by the N,N-dimethyl-p-nitroaniline (RNO) disappearance [28]. RNO is only degraded in the presence of hydroxyl radicals and is not affected by oxy species. A 0.1 mM RNO / 0.03 M Na_2SO_4 solution was prepared and electrolyzed with the same configuration and conditions used in the electrolyses. The evolution of RNO absorbance in the electrolysis was monitored at 440 nm (maximum absorption wavelength for RNO). Samples were removed from the solution at different times, and their absorbance was determined; after that, the sample was returned to the electrochemical cell.

2.5.2. Persulfate ($S_2O_8^{2-}$) determination

Persulfate generation during electrolyses was determined by determining the I_3^- concentration produced during the reaction of $S_2O_8^{2-}$ generated during the electrolysis with an I^- excess (0.5 g KI) [28]. The I_3^- concentration was determined spectroscopically at 353 nm (maximum absorption wavelength for I_3^-) using a quartz cuvette.

2.5.3. Hydrogen peroxide (H_2O_2) determination

H_2O_2 formation was determined using spectrophotometric kits (0.015–6.00 mg/l H_2O_2 Spectroquant®) (Supelco) and determined with a Prove 100 Spectrophotometer (Merck). Since the samples were measured in a 1 cm cuvette and diluted 1:4, the detection limit for H_2O_2 was 0.12 mg/L.

2.5.4. Ozone determination

Ozone generation was determined using the APHA Method 4500-O3 [36], based on the discoloration of a solution of potassium indigotrisulfonate by ozone. The absorbance of potassium indigotrisulfonate was determined at 600 nm with a Prove 100 Spectrophotometer using a 5 cm quartz cuvette.

2.6. Fourier transform infrared spectroscopy with attenuated total reflection (FTIR-ATR)

FTIR-ATR measurements were performed with a Nicolet 6700 Spectrometer equipped with a deuterated triglycine sulfate detector. A horizontal mono-rebound attenuated total reflection was performed using a prism of ZnSe. Spectra were collected with a resolution of 4 cm^{-1}, and 64 scans were averaged. Samples were allowed to dry on the ZnSe prism before the measurements, so the H_2O contribution was minimized.

2.7. Total organic carbon (TOC) and non-purgeable organic carbon (NPOC) determination

TOC and NPOC were determined using a Shimadzu TOC-VCSN analyzer based on the combustion-infrared method. Initial samples and samples after ending the different electrolyses were measured to calculate the TOC and NPOC removal and the extent of NPs mineralization. TOC and NPOC were measured in duplicate.

2.8. Transmission electron microscopy (TEM) and Field emission Scanning electron microscopy (FESEM)

TEM micrographs were obtained using a JEM-1400 Flash transmission electron microscope using an acceleration voltage of 120 kV. A drop of the sample to be observed was deposited on a holey carbon-Au supported copper grid (grid size 200 mesh, hole average diameter 100 nm, Electron Microscopy Sciences) and allowed to dry.

FESEM was used to observe the morphology of the BDD electrodes using an acceleration voltage of 3.0 kV.

3. Results and discussion

3.1. Characterization of the electrodes

The BDD electrodes were characterized with FESEM to observe the morphology of the coating (Fig. S-1). The obtained films are polycrystalline with different crystal sizes and orientations. BDD500 shows the biggest crystallite size (Fig. S.1-a, d, g). The smallest crystallite size was observed for BDD2500 as can be seen in Fig. S.1-b, e, h. BDD10000 had a crystallite size slightly bigger than the one observed for BDD2500 as can be seen in Fig. S.1-c, f, i.

The BDD electrodes with the different boron doping levels were characterized voltammetrically using a 5 mM concentration of two redox mediators ($Ru(NH_3)_6Cl_3$ and $K_3Fe(CN)_6$) and 0.1 M KCl supporting electrolyte. Fig. 1-a shows the voltammetric characterization of the BDD electrodes using the $Ru(NH_3)_6Cl_3$ redox mediator. This redox mediator is an outer-sphere redox marker controlled by simple diffusion, and electron transfer is not influenced by surface characteristics and can be used to differentiate conductivity levels of BDD electrodes [37]. As can be seen, the BDD10000 electrode achieves the highest reversibility (with a peak-to-peak separation (ΔEp) of 97 mV) followed by the BDD500 (ΔEp = 173 mV) and BDD2500 (ΔEp = 195 mV). On the other hand, the $K_3Fe(CN)_6$ redox mediator exhibits an inner-sphere behavior, and its redox reaction is controlled by surface interactions and is strongly dependent on BDD surface properties (surface termination and boron doping level) [37]. With this redox mediator (Fig. 1-b), the BDD10000 electrode was the most reversible one (ΔEp = 96 mV), followed by BDD2500 (ΔEp = 198 mV) and BDD500 (ΔEp = 204 mV), thus showing BDD10000 the fastest electron transfer kinetics. Both redox mediators show faster electron transfer kinetics and the highest current density for the BDD10000 electrode. Similar results have been reported in literature, where the higher the B doping level is, the lower the crystallite size is due to secondary nucleation produced by boron incorporation, and the increased conductivity and electron-transfer activity is obtained [38].

This was clearly observed when the boron doping level was increased from 500 ppm to 2500 ppm (Fig. S.1). In the case of BDD10000, although the crystallite size is slightly bigger than BDD2500, the improved conductivity and electron transfer kinetics must be related to the higher boron doping level.

Fig. 2 shows the linear sweep voltammetry characterization of the BDD electrodes with different B doping levels in 0.03 M and 0.1 M Na_2SO_4 media. The most remarkable fact is that the onset potential for oxygen evolution reaction is higher for 0.1 M Na_2SO_4. In 0.1 M Na_2SO_4, especially for BDD500 and BDD10000, a peak can be observed at around 2 V. In the case of BDD2500, the peak was located at around 1.7 V. This

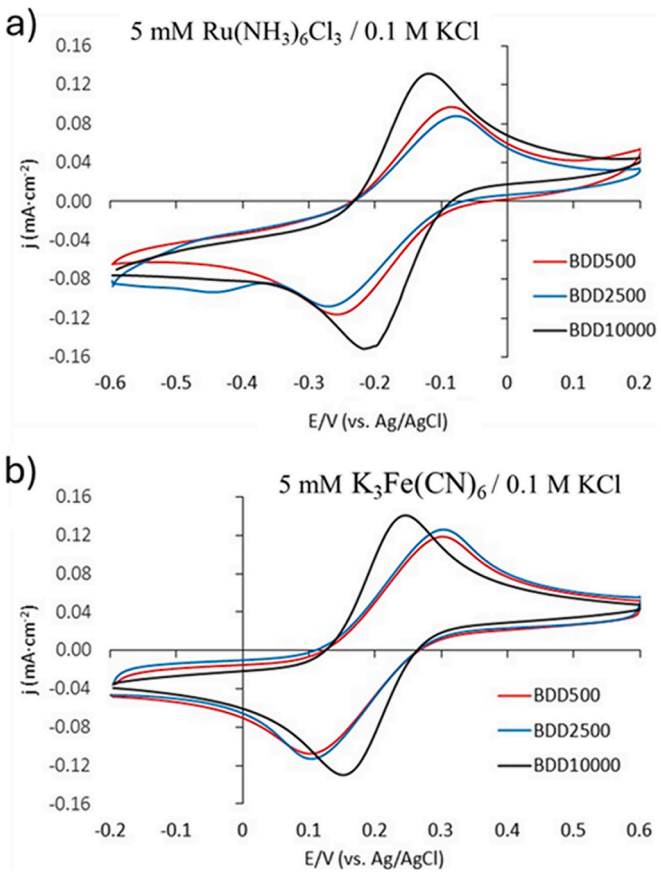

Fig. 1. Cyclic voltammetry characterization of the different electrodes in: a) 0.1 M KCl / 5 mM $Ru(NH_3)_6Cl_3$, b) 0.1 M KCl / 5 mM $K_3Fe(CN)_6$. Scan rate: 50 mV·s^{-1}.

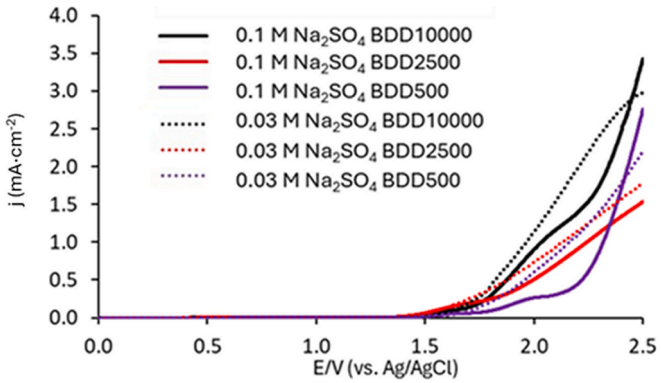

Fig. 2. Linear sweep voltammetry characterization of the different electrodes in 0.03 and 0.1 M Na_2SO_4. Scan rate: 5 mV·s^{-1}.

peak has been attributed to the oxidation of sulfate to form species such as persulfate ions and sulfate radicals with the aid of hydroxyl radicals [39]. For 0.03 M Na_2SO_4, the peaks were not as clearly defined in the former case.

3.2. Linear sweep voltammetry characterization of BDD electrodes in NPs solutions

Fig. 3 shows the linear sweep voltammetry response of the different BDD electrodes in 0.03 M Na_2SO_4 and 0.1 M Na_2SO_4 medium and with different NPs concentrations (0, 20 40, 60, 80, and 100 ppm). The first experiment was performed in 0.03 M Na_2SO_4, adding 20 ppm of NPs sequentially after each measurement until the 100 ppm NPs concentration was achieved.

Fig. 3-a, b shows the characterization of the BDD500 electrode. As can be seen, adding the NPs reduces the current density observed in 0.03 M Na_2SO_4 (Fig. 3-a) and 0.1 M Na_2SO_4 (Fig. 3-b). The effect on the Na_2SO_4 oxidation peak at around 2 V is clearly observed (Fig. 3-b). Thus, the presence of NPs seems to reduce the peak attributed to the sulfate oxidation gradually.

Fig. 3-c, d, show the LSV characterization of the BDD2500 electrode in 0.03 M Na_2SO_4 (Fig. 3-c) and 0.1 M Na_2SO_4 (Fig. 3-d). A similar trend was observed for the BDD2500 electrode, thus observing a reduction of the current density obtained by LSV when NPs were added to the solution.

Fig. 3-e, f show the LSV characterization of the BDD10000 electrode in 0.03 M Na_2SO_4 (Fig. 3-e) and 0.1 M Na_2SO_4 (Fig. 3-f). The current density decreased when NPs were present in the solution was also more marked than when the other electrodes were used. The reduction of the Na_2SO_4 oxidation peak in the 0.1 M Na_2SO_4 medium was also remarkable (Fig. 3-f).

Thus, the presence of NPs in solution seems to influence the electrodes' electroactivity, decreasing the current densities observed for the electrochemical processes such as sulfate oxidation. The practical effects for electrooxidation of NPs in solution mean higher applied potentials to achieve the desired current densities than when only the background electrolyte is present.

To date, no study has reported the influence of NPs concentration on the voltammetric response of BDD or other types of electrodes. Only a previous study by Shimizu et al. reported the usefulness of electrochemical techniques for detecting MPs in water using particle impact electrochemistry [40].

3.3. Electrolyses of nanoplastics in solution

Electrolyses of 20 mg·L^{-1} NPs in 0.03 M Na_2SO_4 aqueous solutions were performed using the different electrodes at different current densities (50, 25, 12.5, and 5 mA·cm^{-2}) to study their influence on the degradation of NPs. The concentration of NPs during electrolysis was monitored using fluorescence spectroscopy, taking advantage of the fluorescence of polystyrene. Fig. 4 shows an example of the evolution of fluorescence spectra during an electrolysis performed at 25 mA·cm^{-2} using a BDD2500 electrode. As can be seen, a gradual decrease of the fluorescence emitted by polystyrene NPs occurs with the increasing electrolysis time, thus evidencing a progressive degradation of NPs.

The degradation of NPs (1) was calculated as the ratio between the intensity of fluorescence at a determined electrolysis time (I_t) and the initial fluorescence of the solution before electrolysis (I_0).

$$Degradation(\%) = \frac{I_0 - I_t}{I_0} x100 \quad (1)$$

Fig. 5-a, b, and c show the degradation of NPs using BDD500, BDD2500, and BDD10000 electrodes, respectively. As can be seen, in general, there is a direct correlation between the current density and the necessary time to achieve a 90 % degradation. Higher current densities generally produce a faster degradation of NPs, as could be expected due to the higher production of reactive oxidizing species that aid their degradation.

Fig. 6-a, b, c, d, compare the degradation of NPs using the different electrodes at 50, 25, 12.5, and 5 mA·cm^{-2}, respectively. Following, we will show the temporal order in which the electrodes with the different doping levels achieve a 90 % degradation at each current density used:

- 50 mA·cm^{-2}: BDD10000 < BDD500 < BDD2500.
- 25 mA·cm^{-2}: BDD2500 < BDD500 < BDD10000.
- 12.5 mA·cm^{-2}: BDD500 < BDD10000 < BDD2500
- 5 mA·cm^{-2}: BDD500 < BDD10000 < BDD2500

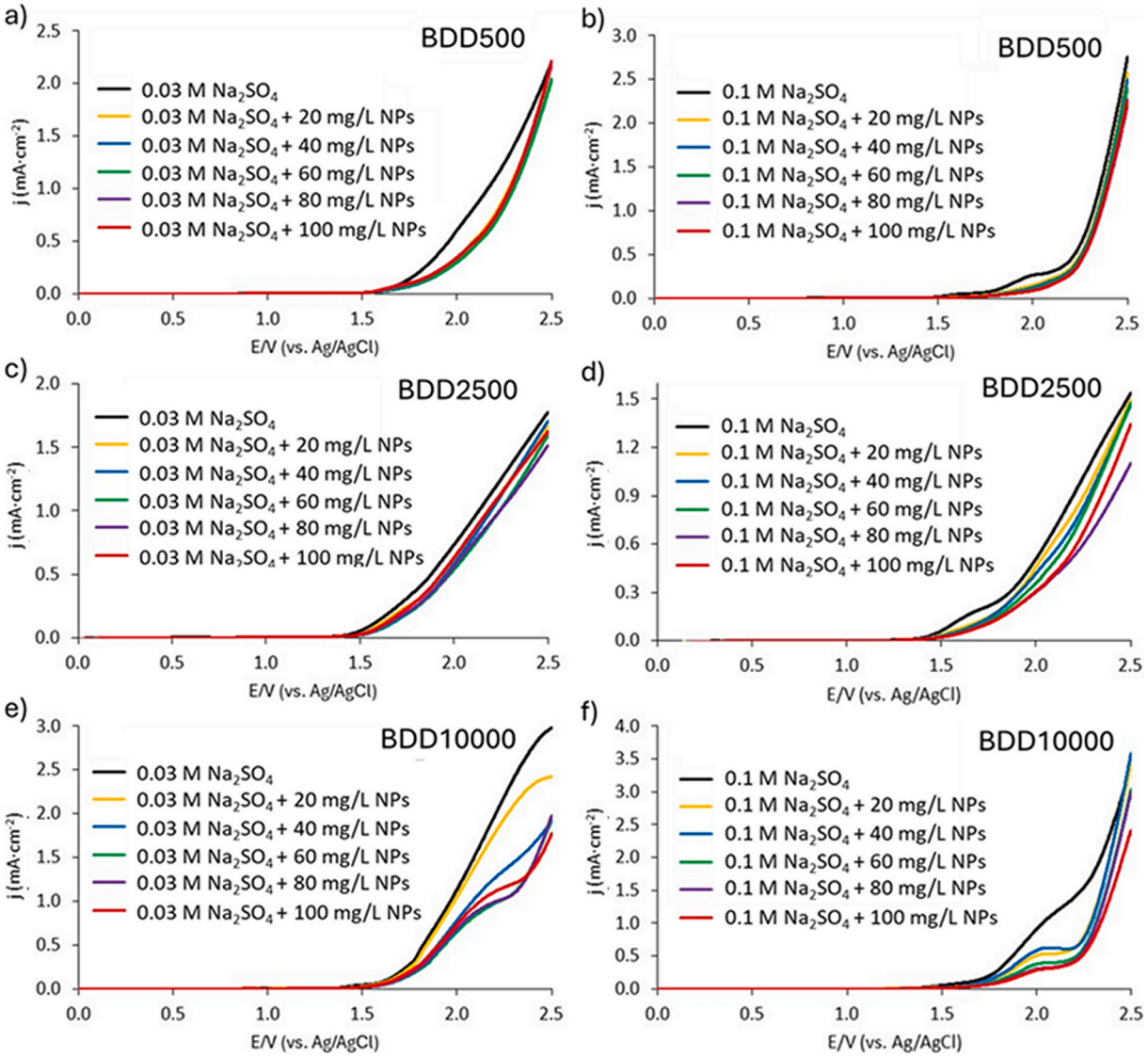

Fig. 3. Linear sweep voltammetry characterization of: (a, b) BDD500, (c, d) BDD2500, and (e, f) BDD10000 electrodes in 0.03 M Na_2SO_4 (a, c, e) and 0.1 M Na_2SO_4 (b, d, f) with different concentration of NPS (0-100 ppm). Scan rate: 5 $mV{\cdot}s^{-1}$.

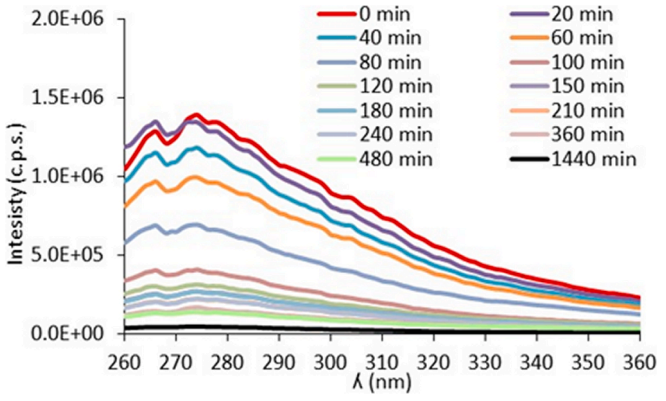

Fig. 4. Evolution of fluorescence spectra of electrolysis of 0.1 μm NPs (20 $mg{\cdot}L^{-1}$) in 0.03 M Na_2SO_4 at 25 $mA{\cdot}cm^{-2}$ using BDD2500 electrode.

Thus, at the highest current density (50 $mA{\cdot}cm^{-2}$), BDD10000 achieves the fastest degradation of NPs, although the results at 360 min are similar for all the electrodes. At 25 $mA{\cdot}cm^{-2}$, BDD2500 is the fastest electrode to degrade NPs. At 12.5 and 5 $mA{\cdot}cm^{-2}$, the BDD500 electrode works better. To further analyze the reason for the behavior of the electrodes, the generation of •OH, $S_2O_8^{2-}$ and H_2O_2 for the different electrodes and the different current densities was monitored with time.

3.4. Determination of oxidative species

3.4.1. Hydroxyl radical

Hydroxyl radical (•OH) is one of the species generated at BDD electrodes, and that promotes the degradation of organic pollutants by advanced oxidation processes [41]. BDD is included in non-active anodes [42], and •OH is generated during water electrolysis on the BDD surface (2), where they are weakly adsorbed and can be released to the solution [38,42].

$$BDD + H_2O \rightarrow BDD\ (\bullet OH) + H^+ + e^- \quad (2)$$

Different methods have been reported to detect •OH: spectrophotometric, fluorescence spectrophotometric, electron spin resonance, high-performance liquid chromatography, etc. [43]. p-nitrosodimethylaniline (RNO) has been widely used for the determination of •OH, since • OH selectively bleaches it and does not react with other reactive species

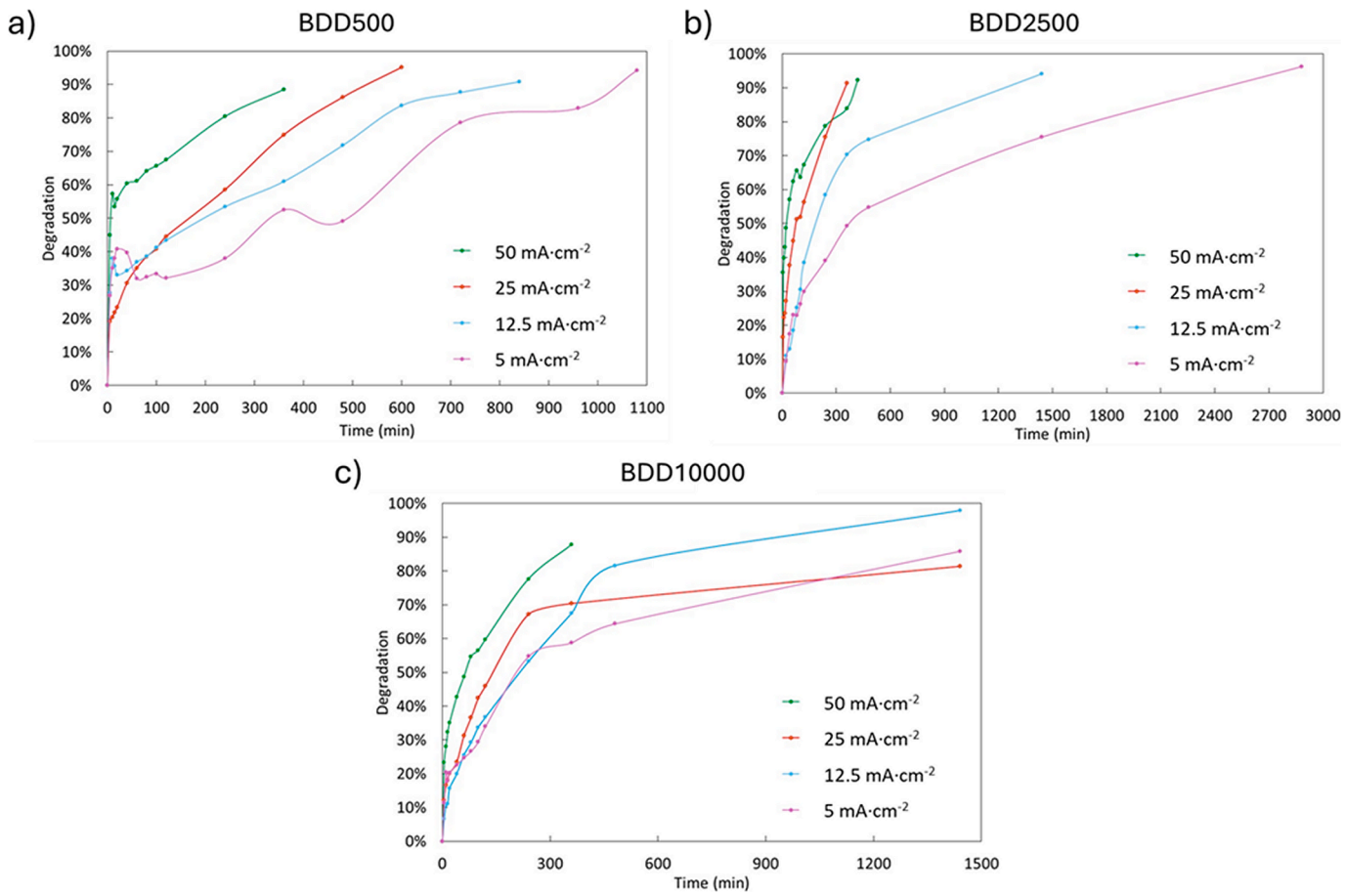

Fig. 5. Evolution of 20 mg/L 100 nm NPs degradation in 0.03 M Na_2SO_4 medium using different electrodes: a) BDD500, b) BDD2500, c) BDD10000 at different current densities: 5, 12.5, 25 and 50 mA·cm^{-2}.

such as superoxide anions, singlet oxygen, and other peroxy compounds [28,44]. However, care should be taken if chloride media is used during electrolysis since chlorine can also bleach RNO by chemical oxidation [44]. In the present study, sulfate media was used to discard Cl_2 generation, so RNO bleaching can only be attributed to •OH generation.

Fig. 7 shows the RNO degradation kinetics by the different BDD electrodes and applied current densities. Pseudo-first-order kinetics were observed for the degradation of RNO by the different BDD electrodes, obtaining an exponential decay of the RNO absorbance with time. This indicates that the limiting step in the RNO degradation is the RNO diffusion to the vicinity of the electrode. It has been reported that the lifetime of •OH is in the order of microseconds [45], and hence, the degradation of RNO occurs in the vicinity of the electrode surface where •OH is generated. The kinetics of RNO bleaching were obtained by representing $\ln(A_t/A_0)$ vs. time (min) [28], where A_t represents the absorbance of the RNO solution at a specific electrolysis time of electrolysis and A_0 represents the initial absorbance of the RNO solution before electrolysis. Fig. 7-a, b, and c show the kinetics of the RNO removal for BDD500, BDD2500, and BDD10000 electrodes, respectively. The •OH formation kinetics is equivalent to the disappearance of RNO since the reaction of RNO with •OH takes place in a 1:1 M ratio [46]. Independently of the B-doping level of BDD electrodes, higher current densities generate more •OH, and the RNO disappearance is fastest. This is also in accordance with data obtained during the electrolyses of NPs, where higher current densities showed the fastest degradation of the NPs.

Table 1 shows the apparent kinetics constants obtained in each case after linear fit performed in Fig. 7-a, b, c. BDD2500 produce the most [•OH] at 50 mA·cm^{-2} and 5 mA·cm^{-2} and BDD10000 at 25 and 12.5 mA·cm^{-2}.

3.4.2. *Hydroxyl radical, indirect generation*

During the experiments with RNO, the appearance of an indirect oxidation process, which contributed to the RNO degradation was also observed. An aliquot was taken at 5 min of electrolysis and its absorbance was monitored until 2 h later (without returning it to the electrochemical cell). It was observed that its absorbance continuously diminished with time. Fig. 8 shows the evolution of the absorbance of the samples taken at 5 min of electrolysis at 50 mA·cm^{-2} with the different electrodes. The initial absorbance of each sample is different since they were taken at 5 min of electrolysis. As can be seen, the effect of indirect RNO degradation is substantial (especially during the first 20 min), which would also undoubtedly contribute to the degradation of NPs.

Ozone can be generated electrochemically on different electrodes [47,48] by reactions (3) and (4) [47]. The potential for O_3 generation reactions is above the oxygen evolution reaction potential (5).

$$3H_2O \rightarrow O_3 + 6H^+ + 6e^- \quad E_0 = 1.511 \text{ V vs. SHE} \tag{3}$$

$$O_2 + H_2O \rightarrow O_3 + 2H^+ + 2e^- \quad E_0 = 2.075 \text{ V vs. SHE} \tag{4}$$

$$2H_2O \rightarrow O_2 + 4H^+ + 4e^- \quad E_0 = 1.229 \text{ V vs. SHE} \tag{5}$$

Ozone has also been reported to bleach RNO [46]. Its half-life in aqueous solution is around 20 min at 20 °C [49], which matches the lifetime of the observed indirect chemical observation. Ozone decomposes according to reaction (6), generating hydroxyl radicals [48]. This reaction depends on pH and is promoted at pH > 6 [48].

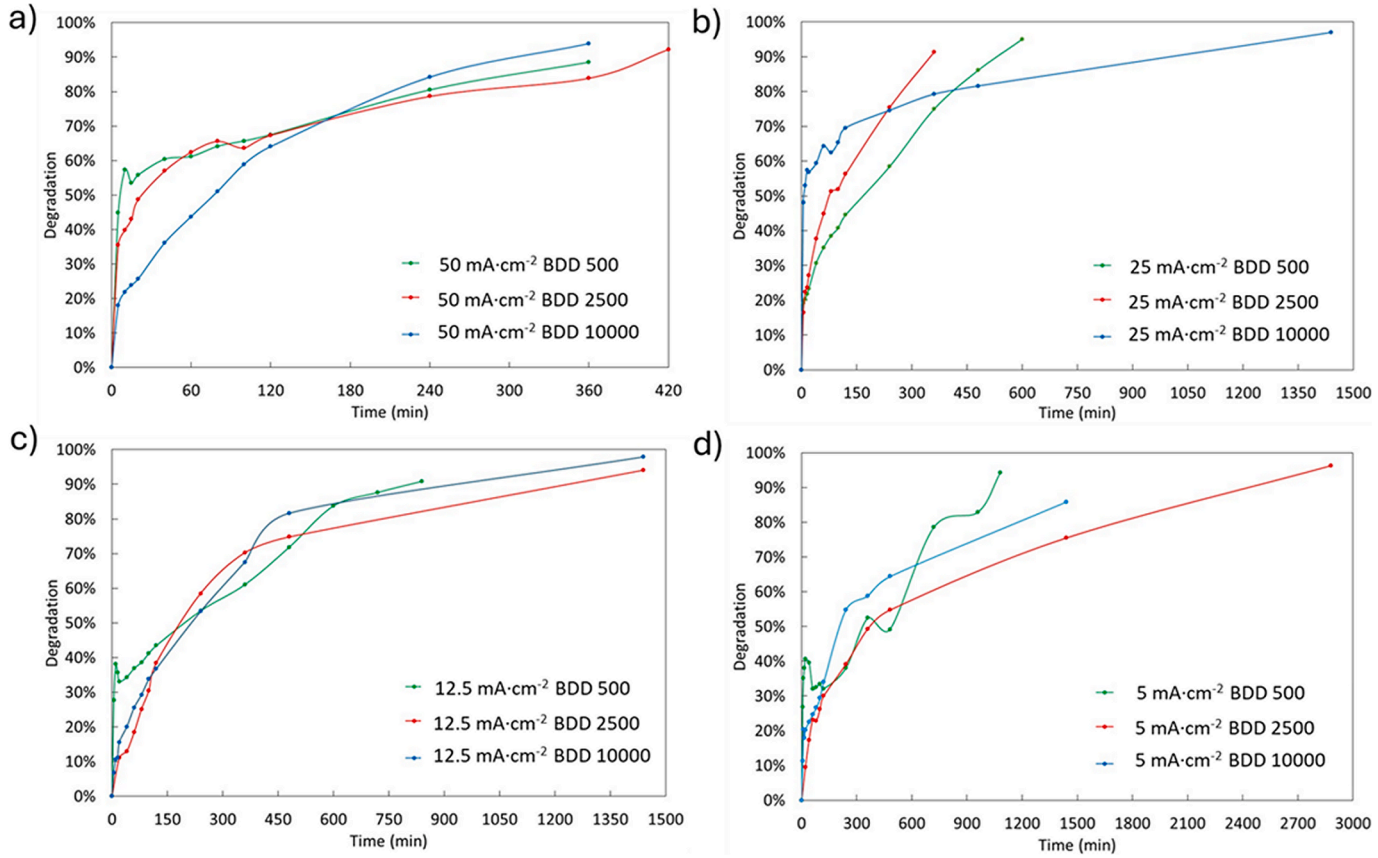

Fig. 6. Evolution of 20 mg/L 100 nm NPs degradation in 0.03 M Na_2SO_4 medium using different electrodes. a) 50 mA·cm^{-2}, b) 25 mA·cm^{-2}, c) 12.5 mA·cm^{-2}, and d) 5 mA·cm^{-2} current densities.

$$O_3 + H_2O \rightarrow O_2 + \bullet OH + OH^- \quad (6)$$

The indirect degradation of RNO could also be caused by the indirect generation of •OH due to chemical reactions between the other oxidants generated during electrolysis that have a lifetime higher than radical species (H_2O_2, $S_2O_8^{2-}$ or O_3). Examples of such reactions are the peroxone reaction [50] (7) or the advanced oxidation processes based on H_2O_2 assisted by persulfate [51] (8).

$$H_2O_2 + 2O_3 \rightarrow 2\bullet OH + 3O_2 \quad (7)$$

$$H_2O_2 + S_2O_8^{2-} \rightarrow 2SO_4^{\bullet -} + 2\bullet OH \quad (8)$$

The effect of the indirect oxidation of RNO is marked in the first minutes, as previously seen, and then it tends to slow down. This is why, when calculating the indirect removal of RNO (or the indirect •OH generation), the data adjusted was limited to 4 min after taking the sample. A pseudo-first-order kinetics model was applied for the direct RNO removal by •OH, and the kinetic constant was determined by adjusting the data linearly. Fig. 9-a, b, c shows the data obtained for BDD500, BDD2500, and BDD10000, respectively. As can be seen, the indirect RNO oxidation kinetic constant increases with the current density (and hence with the applied potential). In the literature, ozone generation has been reported to increase with the increase in the applied potential [52]. The effect is also more marked when the doping level increases. Ozone generation has also been reported to increase when the doping level in BDD electrodes increases [52]. The data obtained indicates that electrogenerated O_3 and its decomposition into •OH could mainly cause the RNO indirect oxidation process.

Table 1 shows the constants obtained for the indirect oxidation of RNO (or the indirect generation of •OH). Table S.1 also shows the ratio between the direct and indirect constants, which can provide a good figure of merit for determining the indirect oxidation contribution. In the BDD10000 electrode for 50 mA·cm^{-2}, this ratio is 1.60, which accounts for a substantial contribution of indirect oxidation. At 5 mA·cm^{-2}, the effect of indirect oxidation is minimal independently of the electrode.

3.4.3. Ozone

To confirm that O_3 was generated and contributed to the indirect degradation of RNO, O_3 was determined using the discoloration of a potassium indigotrisulfonate solution [36]. The analysis was performed in 0.03 M Na_2SO_4 solutions with the different electrodes using 50 mA·cm^{-2}, since at this current density the observed effect of indirect RNO discoloration was more marked. After 5 min of electrolysis, a sample of 90 mL of the electrolyzed solution was mixed with 10 mL of the potassium indigotrisulfonate solution and the absorbance was quantified at 600 nm. The analysis was performed in triplicate for each electrode.

The obtained concentrations of O_3 were 0.18 ± 0.01 μM, 0.13 ± 0.06 μM and 0.06 ± 0.01 μM for BDD10000, BDD2500 and BDD500, respectively. This confirmed the O_3 generation and that the higher the doping level of BDD, the higher the O_3 generation [52].

3.4.4. Persulfate

Electrochemical persulfate generation can be directly performed by sulfate oxidation on the electrodes (Reactions (9) and (10) or indirectly generated by reactions of sulfate with •OH generated at high potentials [53] (Reactions 11–13).

$$2HSO_4^- - 2e^- \rightarrow S_2O_8^{2-} + 2H^+ \quad (9)$$

$$2SO_4^{2-} - 2e^- \rightarrow S_2O_8^{2-} \quad (10)$$

$$H_2O \rightarrow \bullet OH + H^+ + e^- \quad (11)$$

$$HSO_4^- + \bullet OH \rightarrow SO_4^{\bullet -} + H_2O \quad (12)$$

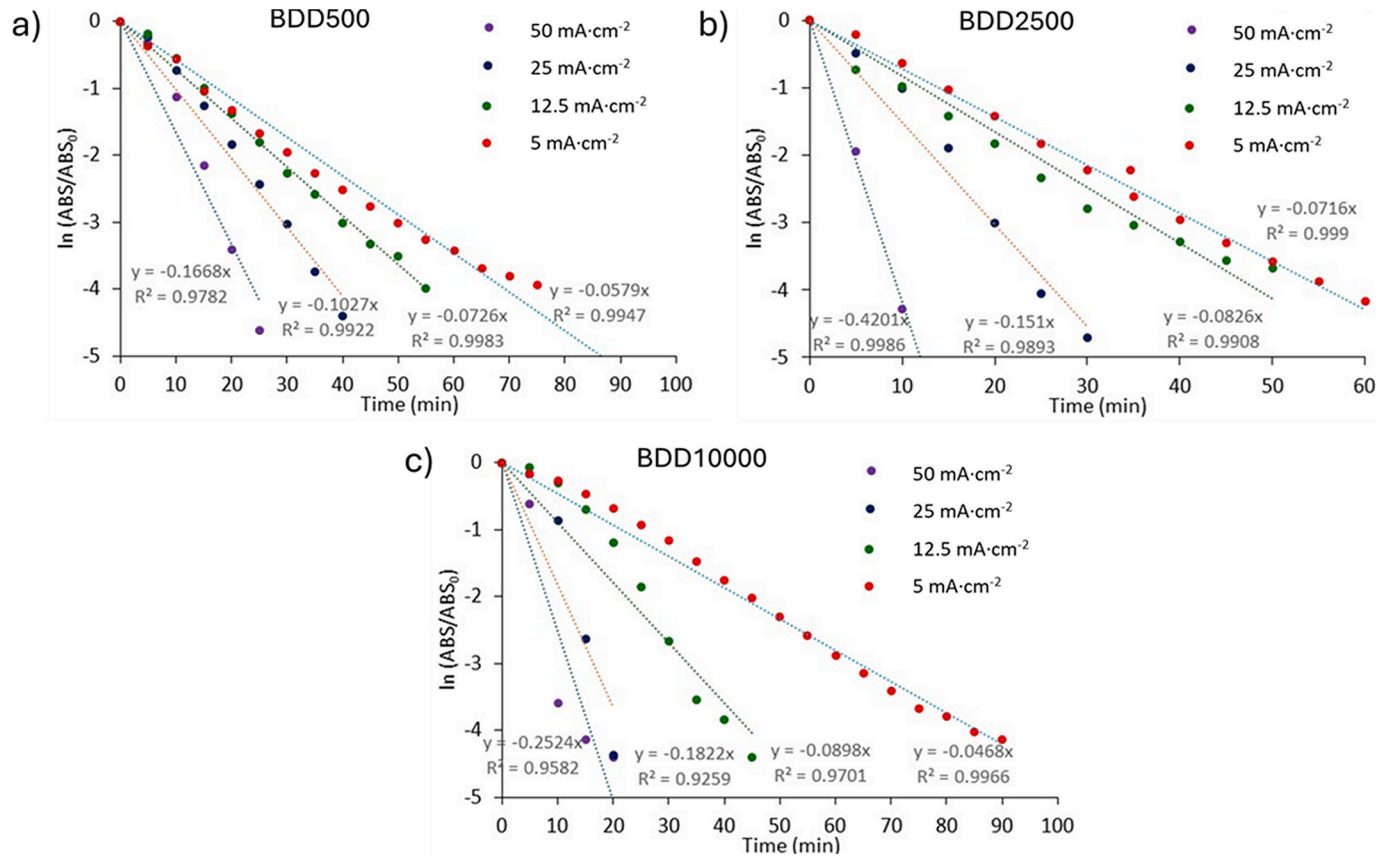

Fig. 7. Kinetics of RNO disappearance using: a) BDD500, b) BDD2500, c) BDD10000. 0.03 M Na_2SO_4 medium and 5, 12.5, 25 and 50 mA·cm^{-2} current densities were applied.

Table 1
Apparent constants for direct (K_{direct}) and indirect ($K_{indirect}$) •OH generation for the different electrodes and the various current densities employed (5, 12.5, 25, and 50 mA·cm^{-2}).

•OH direct production		K_{direct} (min^{-1})		
		Electrode		
		BDD500	**BDD2500**	**BDD10000**
j (mA·cm^{-2})	**5**	0.0579	0.0716	0.0468
	12.5	0.0726	0.0826	0.0898
	25	0.1027	0.151	0.1822
	50	0.1668	0.4201	0.2524
•OH indirect production		$K_{indirect}$ (min^{-1})		
		Electrode		
		BDD500	**BDD2500**	**BDD10000**
j (mA·cm^{-2})	**5**	0.0019	0.0009	0.0014
	12.5	0.0091	0.0164	0.0137
	25	0.0115	0.0307	0.0536
	50	0.0267	0.2068	0.1582

$$2SO_4^{\bullet -} \rightarrow S_2O_8^{2-} \quad (13)$$

Fig. 10-a, b, c, d shows the $[S_2O_8^{2-}]$ evolution during the electrolyses performed with the different electrodes at 50, 25, 12.5, and 5 mA·cm^{-2}, respectively. In general, an increase in current density increases the concentration of persulfate generated. The exception is the 50 mA·cm^{-2} for the BDD500 electrode, which initially rose but then dropped. This could be caused by the rise in the temperature of the solution caused by the resistance of the electrode. The high temperature (57 °C at the end of electrolysis) will undoubtedly contribute to the decomposition of persulfate. This decomposition cannot be discarded on the other electrodes (BDD2500 and BDD10000) but was less marked than on the BDD500 electrode.

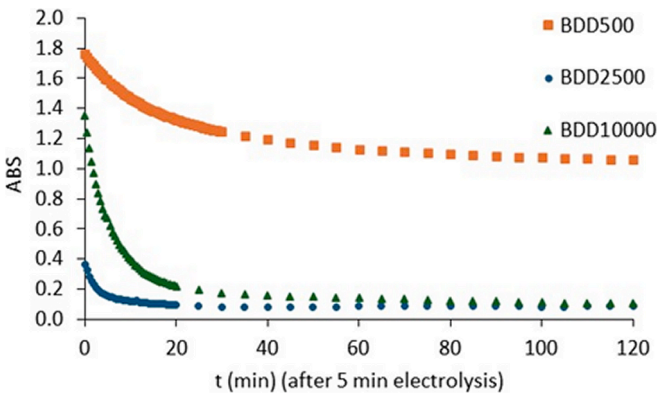

Fig. 8. Evolution of RNO absorbance on samples electrolyzed for 5 min using the different electrodes at 50 mA·cm^{-2}.

In the literature, it has been reported that an increase in B doping in BDD electrodes produces a slight reduction in the persulfate generation when working with 150 g/L Na_2SO_4 [53]. In our study, a lower Na_2SO_4 concentration was used (4.26 g/L), where intermediate doping level (BDD2500) works better for higher current densities (50 and 25 mA·cm^{-2}), and lower doping level (BDD500) works better for lower current densities (12.5 and 5 mA·cm^{-2}).

3.4.5. H_2O_2

H_2O_2 can be generated electrochemically by oxygen reduction

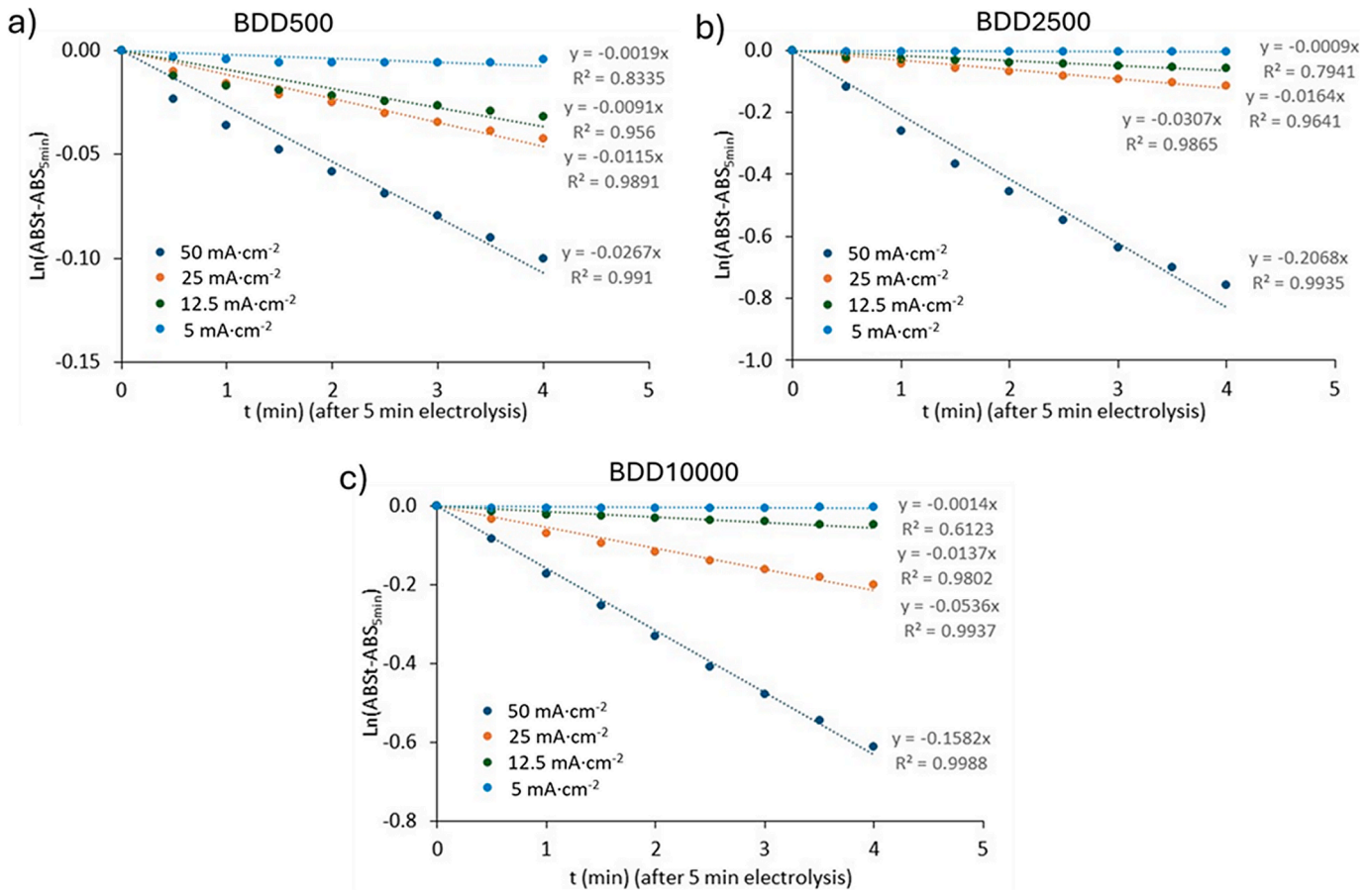

Fig. 9. Kinetics of RNO disappearance in samples taken at 5 min of electrolysis of RNO using: a) BDD500, b) BDD2500, c) BDD10000 electrodes. 0.03 M Na_2SO_4 medium and 5, 12.5, 25 and 50 mA·cm^{-2} current densities.

reaction (14) [54,55]; in this case, the amount of H_2O_2 formed is limited by the amount of dissolved oxygen. The other mechanism of H_2O_2 formation is the water oxidation reaction (15) [54,55]; in this case, the amount of H_2O_2 is only limited by water, which is usually the solvent used in electrolysis.

$$O_{2(g)} + 2e^- + 2H^+ \leftrightarrow H_2O_{2(aq)}\ E_0 = 0.67\ V\ vs.\ RHE \quad (14)$$

$$2H_2O_{(l)} \leftrightarrow H_2O_{2(aq)} + 2H^+ + 2e^-\ E_0 = 1.76\ V\ vs.\ RHE \quad (15)$$

Fig. 11 shows the evolution of H_2O_2 formation for the different electrodes and current densities studied. In general, the BDD500 produces more H_2O_2 than the BDD2500, and this produces more than the BDD10000. The exception is the 5 mA·cm^{-2}, where the 2500 ppm electrode produces more H_2O_2 than the 500 ppm one. An intermediate current density (25 mA·cm^{-2}) produces more H_2O_2 than 50 mA·cm^{-2} for BDD500 and BDD2500 electrodes. In the case of BDD10000, the highest H_2O_2 production rate is obtained at 50 mA·cm^{-2}.

Since the cathode material (Ti plates) was not varied in the study, the differences in H_2O_2 generation can be mainly attributed to the anode material composition, and the predominant mechanism of H_2O_2 formation is the water oxidation reaction pathway (15). With BDD500, H_2O_2 concentration values higher than 10 mg/L were obtained at different times at 50 and 25 mA·cm^{-2}. The solubility of oxygen is around 9 mg/L at 20 °C [56], and during the electrolysis, the temperature rises, which would decrease the dissolved oxygen. This also corroborates the oxidative pathway as the primary mechanism of H_2O_2 formation and the differences observed between the electrodes.

3.4.6. Analysis of the results

Table 2 shows a summary of the time to achieve a ~ 90 % degradation of NPs, the [•OH] during the first 10 min, and the promedium [$S_2O_8^{2-}$] and [H_2O_2] for 210 min.

At 50 mA·cm^{-2}, no substantial differences in the degradation of NPs were observed, being BDD10000 the fastest to degrade NPs, followed by BDD500 and BDD2500. BDD2500 shows the highest •OH and $S_2O_8^{2-}$ production, so the results can only be explained if other oxidants influence the NPs degradation. In the case of BDD10000, which presents the second highest •OH and $S_2O_8^{2-}$ production, the highest O_3 production obtained, could enhance the degradation obtained. BDD500 presents the lowest •OH and $S_2O_8^{2-}$ generation, but H_2O_2 generation is one order of magnitude superior to BDD2500 and BDD10000, which seem to aid in the degradation of NPs.

At 25 mA·cm^{-2}, BDD2500 produces the highest •OH and $S_2O_8^{2-}$ production rate and an intermediate H_2O_2 production, obtaining the fastest kinetics of NPs degradation. The second fastest electrode is BDD500, which produces the lowest •OH, an intermediate $S_2O_8^{2-}$ production, and the highest H_2O_2 production. The slowest electrode is the BDD10000, which produces the lowest amount of $S_2O_8^{2-}$ and H_2O_2 and the second highest amount of •OH.

At 12.5 mA·cm^{-2}, the fastest electrode is the BDD500, with the highest H_2O_2 and $S_2O_8^{2-}$ production rate and the second •OH production. The second fastest electrode is the BDD2500, which presents the highest •OH production but intermediate H_2O_2 and $S_2O_8^{2-}$ production. The slowest electrode is the BDD10000, with the lowest H_2O_2, $S_2O_8^{2-}$ and •OH production.

At 5 mA·cm^{-2}, the fastest electrode is the BDD500, which presents the highest $S_2O_8^{2-}$ production rate and the second •OH and H_2O_2 production rate. The second fastest electrode is BDD10000, which presents the second highest $S_2O_8^{2-}$ production rate but the lowest H_2O_2 and •OH generation. The slowest electrode is BDD2500, which presents the

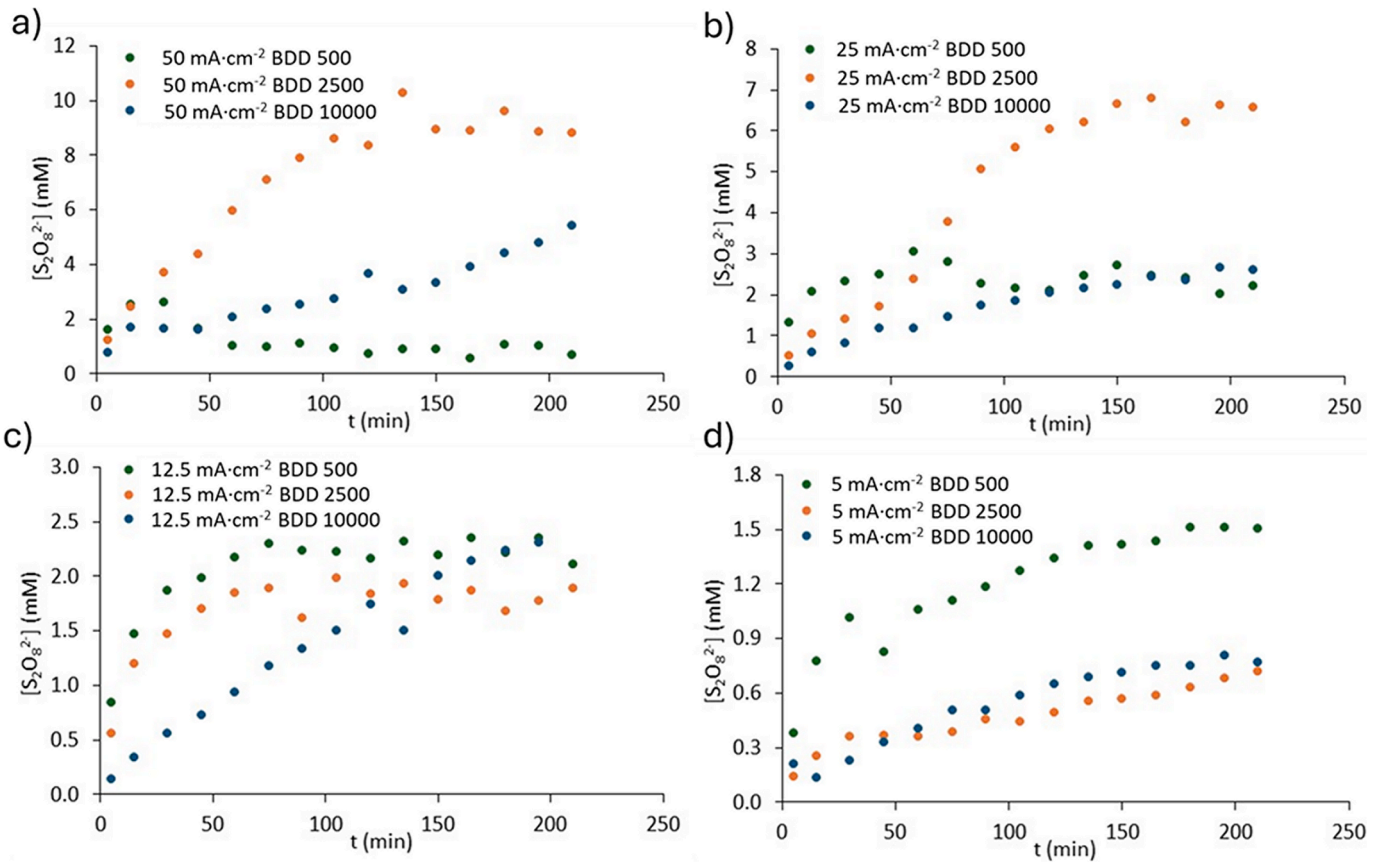

Fig. 10. Evolution of $S_2O_8^{2-}$ concentration during the electrolysis using different current densities with the different electrodes. a) 50 mA·cm^{-2}, b) 25 mA·cm^{-2}, c) 12.5 mA·cm^{-2}, d) 5 mA·cm^{-2}.

highest •OH and H_2O_2 production but the lowest $S_2O_8^{2-}$ production.

After analyzing all the results, at 50 mA·cm^{-2}, the differences observed between the electrodes are slight and cannot directly only be attributed to one factor. At 25, 12.5, and 5 mA·cm^{-2}, it seems that $S_2O_8^{2-}$ production dominates the degradation of NPs by BDD electrodes since the electrodes that produce more $S_2O_8^{2-}$ degrade faster the NPs. It is the reactive oxidizing species generated with the highest concentration, generally several orders of magnitude higher than H_2O_2 and •OH. $S_2O_8^{2-}$ is relatively stable in aqueous solution at room temperature [57]. However, different ways can favor its decomposition: photochemically, sonochemically, thermally, electrochemically, with transition metals, with carbonaceous materials, in alkaline conditions, and with other oxidants such as H_2O_2, O_3, etc. [58]. As reported previously, increasing the solution temperature favors its decomposition and use in removing pollutants. Usually, temperatures between 40–70 °C are used since the half-life of persulfate is limited to hours or even minutes [59]. Persulfate decomposition produces sulfate radicals (16) [59], which will aid in the NPs degradation, or sulfate radicals can react with water to form •OH (17) [59]. As reported previously, oxidants such as H_2O_2 can promote persulfate decomposition (18) [60]. The presence of •OH can also favor the persulfate decomposition and the formation of persulfate radical (19) [61]. Electrochemical activation will undoubtedly play a key role in the decomposition of persulfate (20) [62].

$$S_2O_8^{2-} \rightarrow 2SO_4^{\bullet -} \quad (16)$$

$$2SO_4^{\bullet -} + H_2O \rightarrow SO_4^{2-} + \bullet OH + H^+ \quad (17)$$

$$S_2O_8^{2-} + H_2O_2 \rightarrow 2SO_4^{\bullet -} + 2\bullet OH \quad (18)$$

$$\bullet OH + S_2O_8^{2-} \rightarrow S_2O_8^{\bullet -} + OH^- \quad (19)$$

$$S_2O_8^{2-} + e^- \rightarrow SO_4^{\bullet -} + SO_4^{2-} \quad (20)$$

During electrolysis, the electrode resistance, and the current flow cause an increase in the solution temperature. For example, at 50 mA·cm^{-2}, 57.3, 63.0, and 53.2 °C were obtained for BDD500, BDD2500, and BDD10000, respectively. At lower current densities, the temperature achieved is lower. For example, BDD2500 achieved the highest temperature at 50 mA·cm^{-2}, 46.0, 34.4, and 27.9 °C at 25, 12.5, and 5 mA·cm^{-2}, respectively. Thus, at low current densities, electrochemical decomposition of persulfate will prevail since temperatures lower than 30 °C are not sufficient to allow thermal decomposition [59].

3.5. TEM characterization of NPs before and after electrolysis

Fig. 12-a, b shows polystyrene NPs on the TEM holey carbon grid. As can be seen, the NPs are dispersed over the whole surface of the holey carbon and present a diameter of around 100 nm. Fig. 12-c, d show the NPs after electrolysis; as can be seen in Fig. 12-c, the presence of NPs has been substantially reduced, and only some NPs can be observed in the center of the micrograph. Fig. 12-d shows some NPs that have been partially degraded, losing their spheric shape and diminishing their size (marked with red arrows).

3.6. TOC and NPOC determination

Table 3 shows the measurements of TOC and NPOC for the different electrodes and current densities used. In some cases, there is a significant difference between TOC and NPOC, which can be ascribed to the presence of inorganic carbon species generated during electrooxidation and mineralization of NPs (e.g., CO_2, H_2CO_3, HCO_3^-, CO_3^{2-}). Therefore, NPOC is more significant than TOC in measuring the degradation of NPs. As can be seen, BDD500 produces the highest mineralization at 50, 25, and 12.5 mA·cm^{-2}, achieving values above 80 %, which indicates that

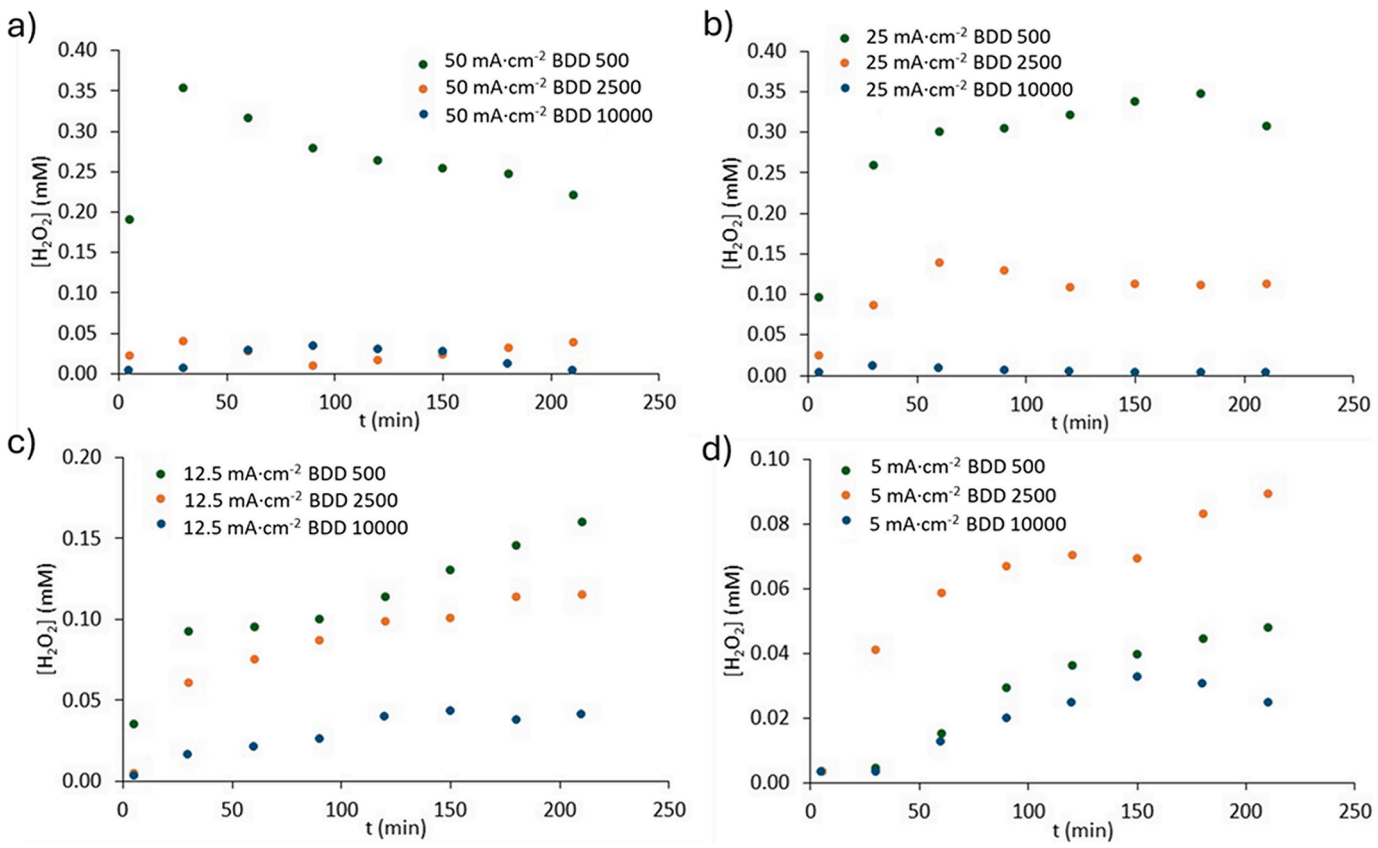

Fig. 11. Evolution of H_2O_2 concentration during the electrolysis using different current densities with the different electrodes. a) 50 mA·cm^{-2}, b) 25 mA·cm^{-2}, c) 12.5 mA·cm^{-2}, d) 5 mA·cm^{-2}.

Table 2
Degradation time, [•OH] during the first 10 min, [$S_2O_8^{2-}$] promedium during 210 min, and [H_2O_2] promedium during 210 min for the different electrodes and the different current densities employed (5, 12.5, 25 and 50 mA·cm^{-2}).

j (mA·cm^{-2})	Electrode	Degradation time (min) (% degrad.)	[•OH] (μM/min) (10 min)	[$S_2O_8^{2-}$] (mM) (prom. 210 min)	[H_2O_2] (mM) (prom. 210 min)
	BDD500	360 (89 %)	6.78	1.21	0.2662
50	BDD2500	420 (92 %)	9.86	7.00	0.0269
	BDD10000	360 (94 %)	9.72	5.21	0.0184
	BDD500	600 (95 %)	5.17	2.33	0.2846
25	BDD2500	360 (91 %)	6.38	4.44	0.1035
	BDD10000	1440 (96 %)	5.81	2.17	0.0057
	BDD500	840 (91 %)	4.27	2.05	0.1092
12.5	BDD2500	1440 (94 %)	6.24	1.67	0.0822
	BDD10000	1440 (98 %)	2.67	1.72	0.0287
	BDD500	1080 (94 %)	4.36	1.18	0.0278
5	BDD2500	2880 (96 %)	4.69	0.47	0.0604
	BDD10000	1440 (86 %)	2.37	0.60	0.0191

intermediates generation is low due to the slight difference between the degradation measured by fluorescence technique and NPOC determination. BDD2500 produced the highest mineralization at 5 mA·cm^{-2} (73 %). The difference between the degradation (%) obtained by fluorescence spectroscopy and the % NPOC reduction was also calculated, following the previously mentioned trend.

3.7. FTIR

Fig. 13 shows the spectra of polystyrene NPs before and after electrolysis (BDD2500 at 25 mA·cm^{-2}). Some of the observed bands are associated with the sulfate used as the electrolyte, and some bands are attributed to polystyrene:

- The peaks at 1450 cm^{-1} and 1425 cm^{-1} could be attributed to the cyclic C–H bond stretching vibration [30], aromatic C=C stretching vibration [63], or aromatic ring modes [64].
- A hump at 1180 cm^{-1} is attributed to HSO_4^- [65].
- A peak at 1130 cm^{-1} is associated with asymmetric SO_3 stretching vibration [65].
- Two peaks, one at 1000 cm^{-1} and another small peak at 910 cm^{-1} are associated with aromatic =CH in-plane deformation vibration [65].
- Two small peaks at 870 cm^{-1} and 830 cm^{-1} are associated with aromatic C–H out-of-plane vibration [63,65,66].
- One small peak at 700 cm^{-1} is associated with the aromatic ring bending [64].

After the electrooxidation of PS NPs, some peaks appear in the spectrum and cannot be assigned to polystyrene. So, they must be associated with the products of the degradation of the surface of the NPs or present in the solution because of the degradation of styrene:

- At 1710 cm^{-1}, a broad band can be observed, which could be identified as the –CH_2COOH group [30].
- A peak at 1365 is associated with the –CH_3 umbrella mode [64].
- A broad peak between 1050–1150 cm^{-1}, overlapped with the band associated with asymmetric SO_3 stretching vibration, associated with C-O stretching vibrations of aliphatic alcohols or ethers, can be observed [65,67]. Nevertheless, it is not discarded that this peak is overlapping with the C–H bending vibration band (usually centered at 1062 cm^{-1}) [68].

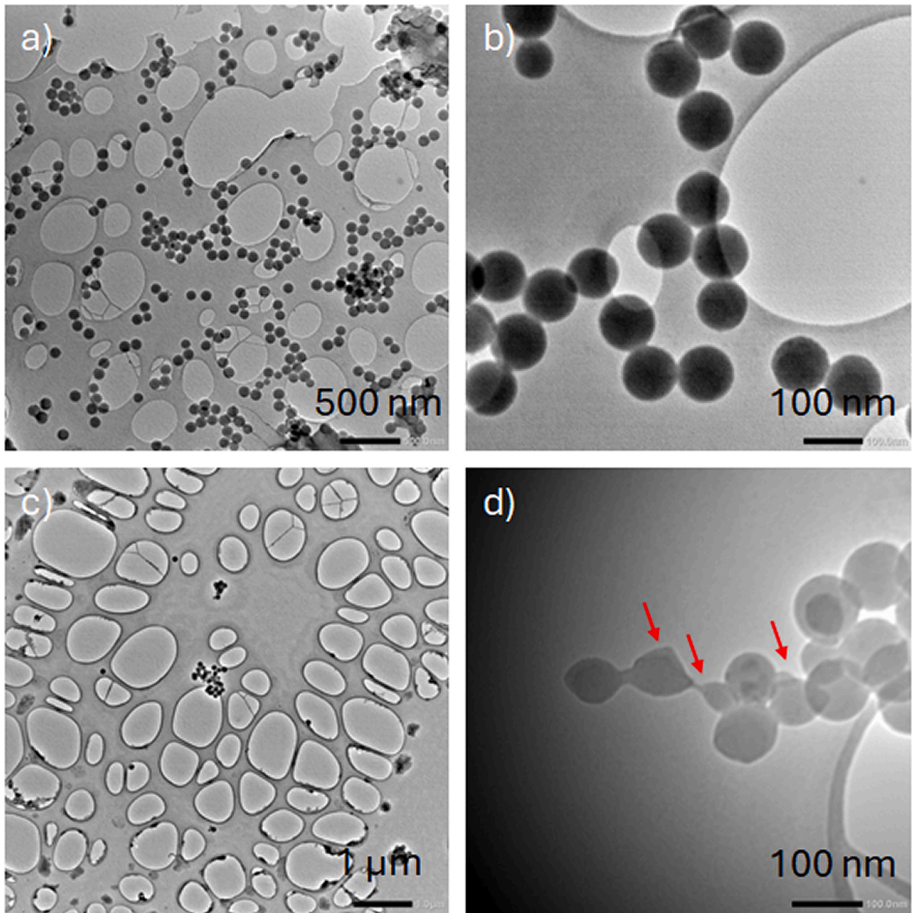

Fig. 12. TEM micrographs of PS NPs before electrolysis (a, b) and after electrolysis (c, d) with BDD500 at 50 mA·cm^{-2}. Magnification: a) x10.000, b) x50.000, c) x5.000, d) x60.000.

Table 3
TOC and NPOC reduction (%) and (% degradation (fluorescence) – % NPOC) for the different experiments.

TOC (% reduction)	Electrode		
j (mA·cm^{-2})	BDD500	BDD2500	BDD10000
50	65.95	73.57	58.21
25	62.75	69.03	45.46
12.5	68.27	69.23	37.73
5	46.38	62.27	57.69
NPOC (% reduction)	**Electrode**		
j (mA·cm^{-2})	BDD500	BDD2500	BDD10000
50	82.81	76.98	81.18
25	85.65	70.71	54.37
12.5	83.59	81.10	54.34
5	58.24	73.35	61.81
% degrad. (fluorescence) – % NPOC reduction	**Electrode**		
j (mA·cm^{-2})	BDD500	BDD2500	BDD10000
50	6.19	15.02	12.82
25	9.35	20.29	41.63
12.5	7.41	12.90	43.66
5	35.76	22.65	24.19

3.8. Evaluation of electrical costs and feasibility

The cost of the treatment of NPs was evaluated according to the electrochemical energy per order (EEO) figure of merit [69] (Table 4):

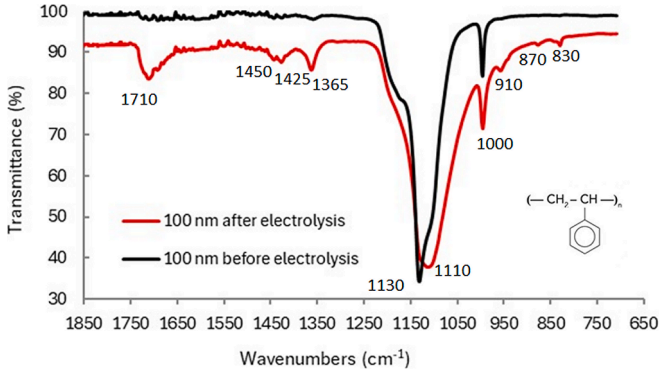

Fig. 13. FTIR spectra of PES NPs before and after electrolysis in 0.03 M Na_2SO_4 (25 mA·cm^{-2}, BDD2500), 64 scans, 4 cm^{-1} resolution.

Table 4
EEO for the different experiments.

EEO (kW·h·m^{-3}·order^{-1})	Electrode		
j (mA·cm^{-2})	BDD500	BDD2500	BDD10000
50	718.6	785.6	506.8
25	401.0	279.5	625.0
12.5	202.5	225.3	202.2
5	64.8	81.9	131.8

$$EEO\left(kW{\cdot}h{\cdot}m^{-3}{\cdot}order^{-1}\right) = \frac{I{\cdot}V{\cdot}t}{Vol{\cdot}\log\frac{C_0}{C}} \quad (21)$$

Where: I is the current intensity (A); V is the average voltage during electrolysis (V); t is the time of electrolysis (h); Vol is the volume of electrolysis (m^3); C_0 is the initial concentration of NPs and C is the final concentration of NPs.

In general, a current density increase produces an increase of treatment's cost, due to parasitic reactions such as oxygen evolution reaction at high overpotentials. On the other hand, the treatment time decreases with the increasing current density. If we consider a cost of 0.15 € kW·h, for example treating a cubic meter with a concentration of 20 mg/L NPs at 12.5 mA·cm^{-2}, the cost would be around 30.4 €/m^3.

This study shows for the first time the importance of selecting the doping level of BDD electrodes to achieve the best results in the degradation of polystyrene NPs. The same study should be performed with other NPs with different structures to determine the influence of the doping level in their degradation. The system is not thought to be applied in high-volume applications and is thought to be applied in batch applications since the residence time to allow the degradation of NPs is above 1 h in all cases. A system could be developed to treat NPs in a tertiary treatment of wastewater treatment plants (combined with nanofiltration) or in laundry wastewater, where NPs are concentrated. During electrolysis, temperature rises as previously reported depending on the current density applied. Once the treatment is finished, the treated solution with high temperature could be mixed with the rest of the wastewater, thus the treated wastewater temperature would be below the limits fixed by legislation.

4. Conclusions

This study shows for the first time the importance of selecting the doping level of BDD electrodes to achieve the best results in the degradation of polystyrene NPs. Boron-doped diamond electrodes with different boron doping levels (500, 2500, and 10000 ppm) have been used to degrade 100-nm polystyrene nanoplastics (PS NPs) in a sulfate medium. The performance of the electrodes in the degradation of NPs has been tested at different current densities (5, 12.5, 25, and 50 mA·cm^{-2}) using fluorescence spectroscopy. Independently of the electrode used, in general the higher the current density, the lower the time for the degradation of NPs. BDD500 achieves the fastest degradation between the electrodes used at 5 and 12.5 mA·cm^{-2}. At 25 mA·cm^{-2}, BDD2500 achieves the fastest degradation, and BDD10000 at 50 mA·cm^{-2}. The different oxidative species generated in the sulfate medium during the electrolyses (•OH, H_2O_2, and $S_2O_8^{2-}$) have been quantified and compared. Independently of the electrode used, $S_2O_8^{2-}$ is generated in a higher concentration than •OH and H_2O_2. Generally, the electrodes that generate more $S_2O_8^{2-}$ at each current density degrade fastest the PS NPs (except for 50 mA·cm^{-2}, where significant differences between the electrodes were not observed). So, the degradation of NPs seems to be commanded by $S_2O_8^{2-}$ generation. $S_2O_8^{2-}$ can be decomposed thermally at high current densities since the solution heats up and electrochemically at all current densities. Direct •OH and H_2O_2 generation seem to contribute to a lower extent in the degradation of NPs than $S_2O_8^{2-}$. In general, the BDD500 electrode produces the highest mineralization at 50, 25, and 12.5 mA·cm^{-2}. The influence of NPs concentration on the linear sweep voltammetry characterization has also been demonstrated, showing a decrease in the electrodes' electroactivity with the increasing NPs concentration.

Role of the funding source

The funding sources had no involvement in the study design; in the collection, analysis and interpretation of data; in the writing of the report; and in the decision to submit the article for publication.

CRediT authorship contribution statement

R. Rodrigo: Investigation, Data curation, Writing – review & editing. **L. Muñoz:** Investigation, Data curation, Writing – review & editing. **J. Bonastre:** Investigation, Data curation, Writing – review & editing. **J. Molina:** Conceptualization, Methodology, Investigation, Data curation, Writing – original draft, Writing – review & editing, Visualization, Supervision. **F. Cases:** Conceptualization, Methodology, Investigation, Data curation, Writing – original draft, Writing – review & editing, Supervision, Project administration, Funding acquisition.

Declaration of competing interest

The authors declare that they have no known competing financial interests or personal relationships that could have appeared to influence the work reported in this paper.

Acknowledgments

This research is part of the Spanish R + D + i contract TED2021-130905B-I00 funded by MCIN/AEI /10.13039/501100011033 and by the European Union NextGenerationEU/PRTR as well as the Red E3Tech Plus: Proyecto Redes de Investigación de la AEI Network E3Tech PLUS (RED2022-134552-T) project. Funding for open access charge: CRUE-Universitat Politècnica de València. The Electron Microscopy Service of the UPV (Universitat Politècnica de València) is gratefully acknowledged for help with TEM and FESEM characterization.

Appendix A. Supplementary material

Supplementary data to this article can be found online at https://doi.org/10.1016/j.seppur.2025.132950.

Data availability

Data will be made available on request.

References

[1] H. Du, Q. Wang, G. Chen, J. Wang, Photo/electro-catalytic degradation of micro- and nano-plastics by nanomaterials and corresponding degradation mechanism, Trends Anal. Chem. 157 (2022) 116815, https://doi.org/10.1016/j.trac.2022.116815.
[2] K. Qian, L. Wang, J. Teng, G. Liu, Strategies and technologies for sustainable plastic waste treatment and recycling, Environ. Funct. Mater (2025), https://doi.org/10.1016/j.efmat.2025.01.004.
[3] B.K. Pramanik, S.K. Pramanik, S. Monira, Understanding the fragmentation of microplastics into nano-plastics and removal of nano/microplastics from wastewater using membrane, air flotation and nano-ferrofluid processes, Chemosphere 282 (2021) 131053, https://doi.org/10.1016/j.chemosphere.2021.131053.
[4] M.S. Bank, Microplastic in the Environment: Pattern and Process, Springer, 2022, https://doi.org/10.1007/978-3-030-78627-4.
[5] P. Kershaw, S. Katsuhiko, J. Leemseth, D. Woodring, Plastic Debris in the Ocean, United Nations Environment Programme (UNEP), UNEP Year Book, 2011, pp. 21–33.
[6] S. Biswas, D. Bagchi, D. Ghosh, The Effects of (Micro and Nano) Plastics on the Human Body: Nervous System, Respiratory System, Digestive System, Placental Barrier, Skin, and Excretory System, in: S. Joo (Ed.), Assessing the Effects of Emerging Plastics on the Environment and Public Health, IGI Global Scientific Publishing, 2022, pp. 148–171, https://doi.org/10.4018/978-1-7998-9723-1.ch008.
[7] Available from: https://ec.europa.eu/commission/presscorner/detail/en/ip_23_4581. Last accessed: 14th February 2025.
[8] J.R. Bermúdez, P.W. Swarzenski, A microplastic size classification scheme aligned with universal plankton survey methods, MethodsX 8 (2021) 101516, https://doi.org/10.1016/j.mex.2021.101516.
[9] M. Kooi, A.A. Koelmans, Simplifying Microplastic via Continuous Probability Distributions for Size, Shape, and Density, Environ. Sci. Technol. Lett. 6 (2019) 551–557, https://doi.org/10.1021/acs.estlett.9b00379.
[10] A. Amobonye, P. Bhagwat, S. Raveendran, S. Singh, S. Pillai, Environmental Impacts of Microplastics and Nanoplastics: A Current Overview, Front. Microbiol. 12 (2021) 768297, https://doi.org/10.3389/fmicb.2021.768297.

[11] T. Wang, M. Hu, G. Xu, H. Shi, J.Y.S. Leung, Y. Wang, Microplastic accumulation via trophic transfer: Can a predatory crab counter the adverse effects of microplastics by body defence? Sci. Total Environ. 754 (2021) 142099 https://doi.org/10.1016/j.scitotenv.2020.142099.
[12] H. Sahai, M.J.M. Bueno, M.M. Gomez-Ramos, A.R. Fernández-Alba, M. D. Hernando, Quantification of nanoplastic uptake and distribution in the root, stem and leaves of the edible herb *Lepidum sativum*, Sci. Total Environ. 912 (2021) 168903, https://doi.org/10.1016/j.scitotenv.2023.168903.
[13] N. Qian, X. Gao, X. Lang, H. Deng, T.M. Bratu, Q. Chen, P. Stapleton, B. Yan, W. Min, Rapid single-particle chemical imaging of nanoplastics by SRS microscopy, PNAS 121 (2024) e2300582121, https://doi.org/10.1073/pnas.2300582121.
[14] M.-S.-L. Yee, L.-W. Hii, C.K. Looi, W.-M. Lim, S.-F. Wong, Y.-Y. Kok, B.-K. Tan, C.-Y. Wong, C.-O. Leong, Impact of Microplastics and Nanoplastics on Human Health, Nanomaterials 11 (2021) 496, https://doi.org/10.3390/nano11020496.
[15] R. Ahmed, A.K. Hamid, S.A. Krebsbach, J. He, D. Wang, Critical review of microplastics removal from the environment, Chemosphere 293 (2022) 133557, https://doi.org/10.1016/j.chemosphere.2022.133557.
[16] S. Miri, R. Saini, S.M. Davoodi, R. Pulicharla, S.K. Brar, S. Magdouli, Biodegradation of microplastics: Better late than never, Chemosphere 286 (2022) 131670, https://doi.org/10.1016/j.chemosphere.2021.131670.
[17] M. Sadia, A. Mahmood, M. Ibrahim, M.K. Irshad, A.H.A. Quddusi, A. Bokhari, M. Mubashir, L.F. Chuah, P.L. Show, Microplastics pollution from wastewater treatment plants: A critical review on challenges, detection, sustainable removal techniques and circular economy, Environ. Technol. Innov. 28 (2022) 102946, https://doi.org/10.1016/j.eti.2022.102946.
[18] T.D. Kusuma, M.S.V. Naga Jyothi, C.P. Rao, S.M. Maliyekkal, Advanced Oxidation Processes: A Promising Route for Abatement of Emerging Contaminants in Water, in: S.P. Singh, K. Rathinam, T. Gupta, A.K. Agarwal (Eds.), Nanomaterials and Nanocomposites for Environmental Remediation, Springer, Singapore, 2021, pp. 275-305. https://doi.org/10.1007/978-981-16-3256-3_12.
[19] J.A. Khan, M. Sayed, S. Khan, N.S. Shah, D.D. Dionysiou, G. Boczkaj, Advanced oxidation processes for the treatment of contaminants of emerging concern, in: A. J. Hernández-Maldonado, L. Blaney (Eds.), Contaminants of Emerging Concern in Water and Wastewater, Butterworth-Heinemann, 2020, pp. 299–365, https://doi.org/10.1016/B978-0-12-813561-7.00009-2.
[20] G. Liu, M. Liu, H. Shi, H. Jia, H. Zou, N. Tao, Efficient electrochemical decomposition of sulfamethoxazole using a novel free-standing TiN anode, Sustainable Horiz. 7 (2023) 100059, https://doi.org/10.1016/j.horiz.2023.100059.
[21] S. Kim, A. Sin, H. Nam, Y. Park, H. Lee, C. Han, Advanced oxidation processes for microplastics degradation: A recent trend, Chem. Eng. J. Adv. 9 (2022) 100213, https://doi.org/10.1016/j.ceja.2021.100213.
[22] Y. Li, J. Li, J. Ding, Z. Song, B. Yang, C. Zhang, B. Guan, Degradation of nano-sized polystyrene plastics by ozonation or chlorination in drinking water disinfection processes, Chem. Eng. J. 427 (2022) 131690, https://doi.org/10.1016/j.cej.2021.131690.
[23] B. Cao, S. Wan, Y. Wang, H. Guo, M. Ou, Q. Zhong, Highly-efficient visible-light-driven photocatalytic H_2 evolution integrated with microplastic degradation over MXene/$Zn_xCd_{1-x}S$ photocatalyst, J. Colloid Interface Sci. 605 (2022) 311–319, https://doi.org/10.1016/j.jcis.2021.07.113.
[24] B. Liu, Q. Jiang, Z. Qiu, L. Liu, R. Wei, X. Zhang, H. Xu, Process analysis of microplastic degradation using activated PMS and Fenton reagents, Chemosphere 298 (2022) 134220, https://doi.org/10.1016/j.chemosphere.2022.134220.
[25] K.B. Možar, M. Milološa, V. Martinjak, M. Cvetnić, H. Kušić, T. Bolanča, D.K. Grgić, Š. Ukić, Potential of Advanced Oxidation as Pretreatment for Microplastics Biodegradation, Separations 10 (2023) 132, https://doi.org/10.3390/separations10020132.
[26] M. Shen, B. Song, C. Zhou, T. Hu, G. Zeng, Y. Zhang, Advanced oxidation processes for the elimination of microplastics from aqueous systems: Assessment of efficiency, perspectives and limitations, Sci. Total Environ. 842 (2022) 156723, https://doi.org/10.1016/j.scitotenv.2022.156723.
[27] R. Bellagamba, P.A. Michaud, Ch. Comninellis, N. Vatistas, Electro-combustion of polyacrylates with boron-doped diamond anodes, Electrochem. Commun. 4 (2002) 171–176, https://doi.org/10.1016/S1388-2481(01)00302-2.
[28] M. Kiendrebeogo, M.R.K. Estahbanati, Y. Ouarda, P. Drogui, R.D. Tyagi, Electrochemical degradation of nanoplastics in water: Analysis of the role of reactive oxygen species, Sci. Total Environ. 808 (2022) 151897, https://doi.org/10.1016/j.scitotenv.2021.151897.
[29] M. Kiendrebeogo, M.R.K. Estahbanati, A.K. Mostafazadeh, P. Drogui, R.D. Tyagi, Treatment of microplastics in water by anodic oxidation: A case study for polystyrene, Environ. Pollut. 269 (2021) 116168, https://doi.org/10.1016/j.envpol.2020.116168.
[30] J. Lu, R. Hou, Y. Wang, L. Zhou, Y. Yuan, Surfactant-sodium dodecyl sulfate enhanced degradation of polystyrene microplastics with an energy-saving electrochemical advanced oxidation process (EAOP) strategy, Water Res. 226 (2022) 119277, https://doi.org/10.1016/j.watres.2022.119277.
[31] L. Mais, N. Melis, A. Vacca, M. Mascia, Electrochemical removal of PET and PE microplastics for wastewater treatment, Environ. Sci.: Water Res. Technol. 10 (2024) 399–407, https://doi.org/10.1039/D3EW00582H.
[32] Z. Ning, X. Duan, Y. Li, X. Zhao, L. Chang, Degradation of polyvinyl chloride microplastics via electrochemical oxidation with a CeO_2–PbO_2 anode, J. Clean. Prod. 432 (2023) 139668, https://doi.org/10.1016/j.jclepro.2023.139668.
[33] F. Miao, Y. Liu, M. Gao, X. Yu, P. Xiao, M. Wang, S. Wang, X. Wang, Degradation of polyvinyl chloride microplastics via an electro-Fenton-like system with a TiO_2/graphite cathode, J. Hazard. Mater. 399 (2020) 123023, https://doi.org/10.1016/j.jhazmat.2020.123023.
[34] W. Sun, G. Liu, H. Zou, S. Wang, X. Duan, Site-designed dual-active-center catalysts for co-catalysis in advanced oxidation processes, npj Mater. Sustain. 3 (2025) 2, https://doi.org/10.1038/s44296-024-00046-4.
[35] W. Sun, Y. Zhou, M. Liu, Y. Tian, H. Zou, X. Duan, H. Jia, G. Liu, Overcome the trade-off in electro-fenton chemistry for in situ H_2O_2 generation-activation by tandem CoFe bimetallic single-atom configuration, Appl. Catal. B-Environ. Energy 357 (2024) 124320, https://doi.org/10.1016/j.apcatb.2024.124320.
[36] 4500-O3. Indigo Colorimetric Method, APHA (1992) Standard Methods for the Examination of Water and Wastewater. 18th Edition, American Public Health Association, Washington DC.
[37] Z. Liu, S. Baluchová, A.F. Sartori, Z. Li, Y. Gonzalez-Garcia, M. Schreck, J. G. Buijnsters, Heavily boron-doped diamond grown on scalable heteroepitaxial quasi-substrates: A promising single crystal material for electrochemical sensing applications, Carbon 201 (2023) 1229–1240, https://doi.org/10.1016/j.carbon.2022.10.023.
[38] G.O.S. Santos, K.I.B. Eguiluz, G.R. Salazar-Banda, C. Sáez, M.A. Rodrigo, Understanding the electrolytic generation of sulfate and chlorine oxidative species with different boron-doped diamond anodes, J. Electroanal. Chem. 857 (2020) 113756, https://doi.org/10.1016/j.jelechem.2019.113756.
[39] S.W. da Silva, E.M.O. Navarro, M.A.S. Rodrigues, A.M. Bernardes, V. Pérez-Herranz, Using p-Si/BDD anode for the electrochemical oxidation of norfloxacin, J. Electroanal. Chem. 832 (2019) 112–120, https://doi.org/10.1016/j.jelechem.2018.10.049.
[40] K. Shimizu, S.V. Sokolov, E. Kätelhön, J. Holter, N.P. Young, R.G. Compton, In situ Detection of Microplastics: Single Microparticle-electrode Impacts, Electroanalysis 29 (2017) 1–9, https://doi.org/10.1002/elan.201700213.
[41] Z.U.H. Khan, N.S. Gul, S. Sabahat, J. Sun, K. Tahir, N.S. Shah, N. Muhammad, A. Rahim, M. Imran, J. Iqbal, T.M. Khan, S. Khasim, U. Farooq, J. Wu, Removal of organic pollutants through hydroxyl radical-based advanced oxidation processes, Ecotoxicol. Environ. Saf. 267 (2023) 115564, https://doi.org/10.1016/j.ecoenv.2023.115564.
[42] C.A. Martínez-Huitle, M.A. Rodrigo, I. Sirés, O. Scialdone, Single and Coupled Electrochemical Processes and Reactors for the Abatement of Organic Water Pollutants: A Critical Review, Chem. Rev. 115 (2015) 13362–13407, https://doi.org/10.1021/acs.chemrev.5b00361.
[43] C. Huang, Q. Chen, S. Li, J. Wang, The Detection Methods of Hydroxyl Radical: A Review, in: E3S Web of Conferences, 375, 2023, p. 03009, https://doi.org/10.1051/e3sconf/202337503009.
[44] J. Muff, L.R. Bennedsen, E.G. Søgaard, Study of electrochemical bleaching of p-nitrosodimethylaniline and its role as hydroxyl radical probe compound, J. Appl. Electrochem. 41 (2011) 599–607, https://doi.org/10.1007/s10800-011-0268-1.
[45] P. Attri, Y.H. Kim, D.H. Park, J.H. Park, Y.J. Hong, H.S. Uhm, K.-N. Kim, A. Fridman, E.H. Choi, Generation mechanism of hydroxyl radical species and its lifetime prediction during the plasma-initiated ultraviolet (UV) photolysis, Sci. Rep. 5 (2015) 9332, https://doi.org/10.1038/srep09332.
[46] M.E. Simonsen, J. Muff, L.R. Bennedsen, K.P. Kowalski, E.G. Søgaard, Photocatalytic bleaching of p-nitrosodimethylaniline and a comparison to the performance of other AOP technologies, J. Photochem. Photobiol. A: Chem. 216 (2010) 244–249, https://doi.org/10.1016/j.jphotochem.2010.07.008.
[47] J. Liu, X. Peng, X. Wang, X. Zhong, J. Wang, Electrochemical ozone production: from fundamental mechanisms to advanced applications, EES. Catal. (2025), https://doi.org/10.1039/d4ey00204k.
[48] M. Rodríguez-Peña, J.A. Barrios Pérez, J. Llanos, C. Sáez, M.A. Rodrigo, C. E. Barrera-Díaz, New insights about the electrochemical production of ozone, Curr. Opin. Electrochem. 27 (2021) 100697, https://doi.org/10.1016/j.coelec.2021.100697.
[49] F.A. Miller, C.L.M. Silva, T.R.S. Brandão, A Review on Ozone-Based Treatments for Fruit and Vegetables Preservation, Food Eng. Rev. 5 (2013) 77–106, https://doi.org/10.1007/s12393-013-9064-5.
[50] G. Acosta-Santoyo, L.F. León-Fernández, E. Bustos, P. Cañizares, M.A. Rodrigo, J. Llanos, On the production of ozone, hydrogen peroxide and peroxone in pressurized undivided electrochemical cells, Electrochim. Acta 390 (2021) 138878, https://doi.org/10.1016/j.electacta.2021.138878.
[51] W. Song, J. Li, X. Zhang, J. Feng, X. Du, Q. Wang, C. Fu, W. Qiu, Z. Wang, X. Gao, A feasible approach for azo-dye methyl orange degradation in siderite/ H_2O_2 assisted by persulfate: Optimization using response surface methodology and pathway, J. Environ. Manage. 308 (2022) 114397, https://doi.org/10.1016/j.jenvman.2021.114397.
[52] Y. Honda, T.A. Ivandini, T. Watanabe, K. Murata, Y. Einaga, An electrolyte-free system for ozone generation using heavily boron-doped diamond electrodes, Diam. Relat. Mater. 40 (2013) 7–11, https://doi.org/10.1016/j.diamond.2013.09.001.
[53] Y. Zhou, D. Liu, G. Sun, Y. Xu, H. Zhao, Boron doped diamond electrode for efficient persulfate generation: The modulation of boron doping level on interfacial electron transfer, Chem. Eng. Sci. 281 (2023) 119123, https://doi.org/10.1016/j.ces.2023.119123.
[54] P.J. Espinoza-Montero, P. Alulema-Pullupaxi, B.A. Frontana-Uribe, C.E. Barrera-Diaz, Electrochemical production of hydrogen peroxide on Boron-Doped diamond (BDD) electrode, Curr. Opin. Solid State Mater. Sci. 26 (2022) 100988, https://doi.org/10.1016/j.cossms.2022.100988.
[55] S. Mavrikis, M. Göltz, S.C. Perry, F. Bogdan, P.K. Leung, S. Rosiwal, L. Wang, C. Ponce de León, Effective Hydrogen Peroxide Production from Electrochemical Water Oxidation, ACS Energy Lett. 6 (2021) 2369–2377, https://doi.org/10.1021/acsenergylett.1c00904.
[56] https://www.engineeringtoolbox.com/oxygen-solubility-water-d_841.html. Last accessed: 28/01/2025.

[57] X. Li, G. Fang, L. Chen, R. Guo, D. Zou, Y. Liu, Optimization of thermally activated persulfate pretreatment of corn straw and its effect on anaerobic digestion performance and stability, Biomass Bioenergy 154 (2021) 106216, https://doi.org/10.1016/j.biombioe.2021.106216.
[58] X. Duan, S. Yang, S. Wacławek, G. Fang, R. Xiao, D.D. Dionysiou, Limitations and prospects of sulfate-radical based advanced oxidation processes, J. Environ. Chem. Eng. 8 (2020) 103849, https://doi.org/10.1016/j.jece.2020.103849.
[59] O.S. Arvaniti, A.A. Ioannidi, D. Mantzavinos, Z. Frontistis, Heat-activated persulfate for the degradation of micropollutants in water: A comprehensive review and future perspectives, J. Environ. Manag. 318 (2022) 115568, https://doi.org/10.1016/j.jenvman.2022.115568.
[60] R. Qiu, P. Zhang, G. Feng, X. Ni, Z. Miao, L. Wei, H. Sun, Enhanced thermal activation of persulfate by coupling hydrogen peroxide for efficient degradation of pyrene, Chemosphere 303 (2022) 135057, https://doi.org/10.1016/j.chemosphere.2022.135057.
[61] C. Zhu, F. Zhu, C. Liu, N. Chen, D. Zhou, G. Fang, J. Gao, Reductive Hexachloroethane Degradation by $S_2O_8^{\bullet-}$ with Thermal Activation of Persulfate under Anaerobic Conditions, Environ. Sci. Technol. 52 (2018) 8548–8557, https://doi.org/10.1021/acs.est.7b06279.
[62] A. Fernandes, M.J. Nunes, A.S. Rodrigues, M.J. Pacheco, L. Ciríaco, A. Lopes, Electro-Persulfate Processes for the Treatment of Complex Wastewater Matrices: Present and Future, Molecules 26 (2021) 4821, https://doi.org/10.3390/molecules26164821.
[63] F. JunFei, X. YiMin, L. Qiang, Preparation of polystyrene spheres in different particle sizes and assembly of the PS colloidal crystals, Sci. China. Technol. Sci. 53 (2010) 3088–3093, https://doi.org/10.1007/s11431-010-4110-5.
[64] B.C. Smith, The Infrared Spectra of Polymers III: Hydrocarbons Polymers, Spectroscopy 36 (2021) 22–25, https://doi.org/10.56530/spectroscopy.mh7872q7.
[65] G. Socrates, Infrared Characteristic Group Frequencies, second ed., John Wiley & Sons Inc, Chichester, 1997.
[66] K. Nishikida, J. Coates, Infrared and Raman Analysis of Polymers, in: H. Lobo, J. V. Bonilla (Eds.), Handbook of Plastics Analysis, Marcel and Dekker Inc, New York, 2003.
[67] Available from: https://kpu.pressbooks.pub/organicchemistry/chapter/6-3-ir-spectrum-and-characteristic-absorption-bands/. Last accessed: 14th February 2025.
[68] M.F.H. Al-Kadhemy, W.H. Abaas, I. Fakher, The Effect of Gamma Radiation on the FTIR Spectrum of Crystal Violet Doped Polystyrene Films, Casp. J. Appl. Sci. Res. 2 (2013) 11–17.
[69] H. Hamous, A. Khenifi, F. Orts, J. Bonastre, F. Cases, Carbon textiles electrodes modified with RGO and Pt nanoparticles used for electrochemical treatment of azo dye, J. Electroanal. Chem. 887 (2021) 115154, https://doi.org/10.1016/j.jelechem.2021.115154.